Letters

Inset Microstripline-Fed Circularly Polarized Microstrip Antennas

Wen-Shyang Chen, Kin-Lu Wong, and Chun-Kun Wu

***Abstract*—Circular polarization (CP) designs of inset microstripline-fed microstrip antennas are proposed. Three designs with a single slit, two pairs of slits, and three pairs of slits are experimentally studied. Good CP performances of the proposed antennas are achieved. For the design with three pairs of slits studied here, the center CP frequency is also seen to be lowered by about 33% compared to the case without slits, which suggests that an antenna size reduction as large as 55% can be obtained if the proposed design is used in place of a conventional CP design at a fixed frequency.**

***Index Terms*—Circular polarization (CP), inset microstripline-fed, microstrip antenna.**

I. Introduction

Microstrip antennas directly excited using a 50-Ω inset microstripline have the advantage of no external impedance transformer required and are very suitable for applications in integration with associated coplanar microwave circuitry. However, related designs with an inset microstripline feed are mainly for achieving linear polarization operations [1] and, to the authors' knowledge, the designs of inset microstripline-fed circularly polarized microstrip antennas are not available in the open literature.

In this paper, we propose new CP designs for exciting a circularly polarized microstrip antenna using a 50-Ω inset microstripline. The main problem to be solved is the perturbation effects caused by the inset microstripline on the excited patch surface current, which makes it difficult for the excitation of two orthogonal near-degenerate resonant modes for CP radiation. It is found that by inserting a single slit or pairs of slits at the patch edges (see Fig. 1), the excitation of two orthogonal near-degenerate modes for CP radiation becomes easy to be achieved. Details of the proposed designs applied to a corner-truncated square microstrip antenna are presented.

II. Antenna Designs

Three proposed designs are shown in Fig. 1. Fig. 1(a) shows the case with a narrow slit (denoted as design A here); Fig. 1(b) is for the case with two pairs of slits (design B); and the design in Fig. 1(c) is with three pair of inserted slits (design C). The 50-Ω inset microstrip line has a width w_c and an inset length ℓ_t. All the inserted slits are of length ℓ_s and width 1 mm and the pairs of slits in Fig. 1(b) and (c) are also with a distance d apart. The square patch has a side length L and a pair of truncated corners of dimensions $\Delta L \times \Delta L$. Because of the combined effects of the inset microstripline and the slits, two orthogonal near-degenerate modes for CP radiation can easily be excited. Also, the excited patch surface currents are meandered in the proposed designs, and the obtained center CP frequency will greatly be lowered, compared to a probe-fed truncated-square microstrip antenna [2]. That is, compact CP radiation [3]–[5] can be achieved for the proposed designs.

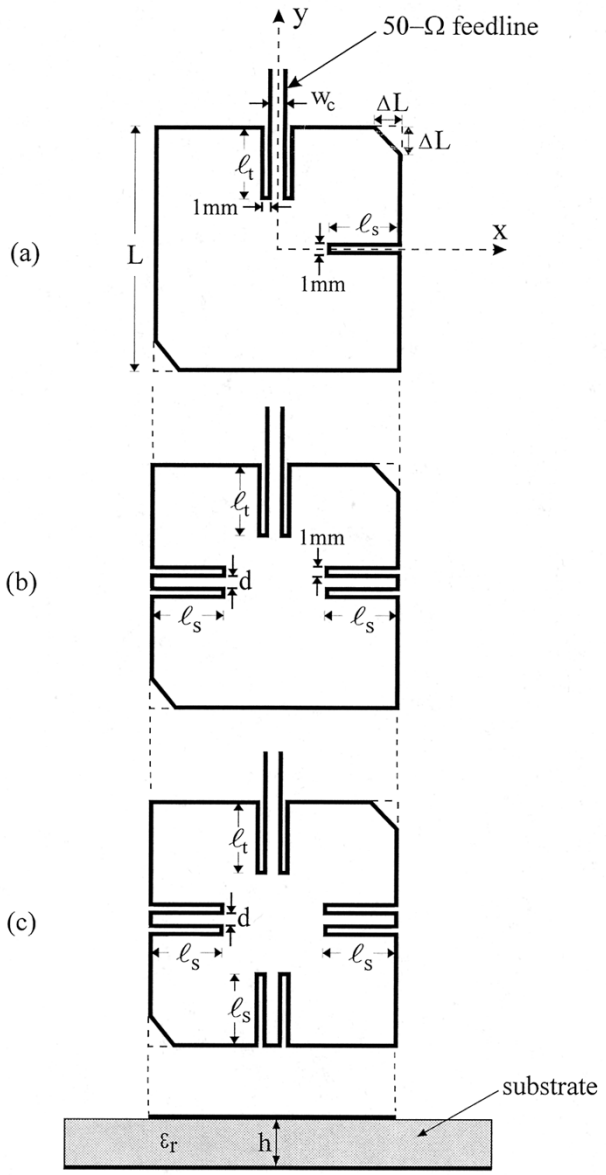

Fig. 1. Geometry of the proposed inset microstripline-fed microstrip antennas for circular polarization. (a) Design A: the corner-truncated square patch with a slit. (b) Design B: the corner-truncated square patch with two pairs of slits. (c) Design C: the corner-truncated square patch with three pairs of slits. The antennas are all with right-hand CP radiation.

III. Experimental Results and Discussion

A probe-fed circularly polarized truncated-square microstrip antenna [2] is first constructed as a reference antenna. The dimensions of truncated corners, the CP bandwidth, and the center CP frequency (f_c; defined here as the frequency with minimum axial ratio in the CP bandwidth) are shown in Table I. Fig. 2 presents the measured input

Manuscript received February 11, 1999; revised January 12, 2000.

W.-S. Chen is with the Department of Electronic Engineering, Cheng-Shiu Institute of Technology, Kaohsiung, Taiwan 873, R.O.C.

K.-L. Wong and C.-K. Wu are with the Department of Electrical Engineering, National Sun-Yat Sen University, Kaohsiung, Taiwan 804, R.O.C.

Publisher Item Identifier S 0018-926X(00)07695-X.

TABLE I
CP PERFORMANCES FOR THE PROPOSED INSET MICROSTRIPLINE-FED MICROSTRIP ANTENNAS; $L = 28$ mm, $\varepsilon_r = 4.4$, $h = 1.6$ mm, $w_c = 3.0$ mm

	ℓ_s (mm)	d (mm)	ℓ_t (mm)	ΔL (mm)	f_c (MHz)	CP Bandwidth (3-dB axial ratio)
Design A	9.7	----	7.4	3.3	2183	0.8%
Design B	9.8	3.0	10.8	3.6	1775	0.8%
Design C	10.8	3.0	10.8	3.9	1653	0.7%
Reference	----	----	----	3.2	2480	1.4%

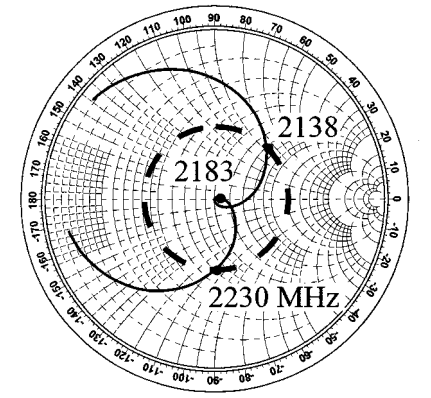

(a)

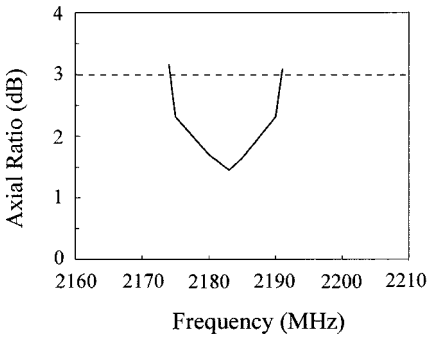

(b)

Fig. 2. Measured (a) input impedance and (b) axial ratio in the broadside direction of the proposed antenna (design A) in Fig. 1(a); $L = 28$ mm, $\Delta L = 3.3$ mm, $\varepsilon_r = 4.4$, $h = 1.6$ mm, $\ell_s = 9.7$ mm, $\ell_t = 7.4$ mm, $w_c = 3.0$ mm, ground-plane size $= 60 \times 60$ mm^2.

impedance and axial ratio of design A, and the corresponding results along with the design parameters are given in Table I. The design parameters can be obtained from the simulation software IE3D.[1] Two near-degenerate resonant modes with good impedance matching are excited [see Fig. 2(a)], and the CP bandwidth [see Fig. 2(b); determined by 3-dB axial ratio] is 17 MHz or about 0.8% with respect to the center frequency at 2183 MHz. Note that the center frequency is lowered by about 12% as compared to that (2480 MHz) of the reference antenna. This can correspond to an antenna size reduction of about 23% for using design A in place of the reference antenna at a fixed frequency. Measured radiation patterns are plotted in Fig. 3 and good right-hand CP radiation is obtained.

For designs B and C, related parameters can also be obtained from IE3D and are given in Table I. It is found that the center CP frequencies of designs B and C occur, respectively, at 1775 and 1653 MHz, lowered

[1]IE3D is a trademark.

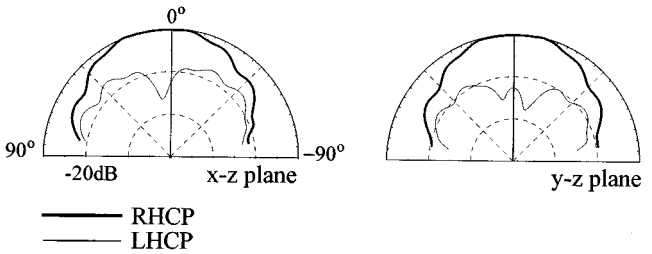

Fig. 3. Measured radiation patterns in two orthogonal planes for the antenna shown in Fig. 2 with $f = 2183$ MHz.

by about 28% and 33% compared to that of the reference antenna. That is, an antenna size reduction about 49% or 55% can be expected at a fixed frequency by replacing the reference antenna with design B or C. Also, from measured radiation patterns of designs B and C, good CP radiation is observed.

IV. CONCLUSION

Novel inset microstripline-fed circularly polarized microstrip antennas with corner-truncated square patches have been proposed and implemented. In addition to good CP radiation obtained, a large antenna size reduction for operating at a fixed frequency can be obtained by using the proposed antennas in place of the conventional CP antennas with simple patches [2] and, although only the designs with corner-truncated square patches are demonstrated, the proposed designs are expected to be applicable to other promising patches such as a circular patch with a pair of peripheral cuts [4] or with a tuning stub [6].

REFERENCES

[1] K. Chang, *Handbook of Microwave and Optical Components*. New York: Wiley, 1989, vol. 1.
[2] P. C. Sharma and K. C. Gupta, "Analysis and optimized design of single feed circularly polarized microstrip antenna," *IEEE Trans. Antennas Propagat.*, vol. AP-31, pp. 949–955, 1983.
[3] K. L. Wong and J. Y. Wu, "Single-feed small circularly polarized square microstrip antenna," *Electron. Lett.*, vol. 33, pp. 1833–1834, 1997.
[4] W. S. Chen, C. K. Wu, and K. L. Wong, "Compact circularly-polarized circular microstrip antenna with cross-slot and peripheral cuts," *Electron. Lett.*, vol. 34, pp. 1040–1041, 1998.
[5] ——, "Single-feed square-ring microstrip antenna with truncated corners for compact circular polarization operation," *Electron. Lett.*, vol. 34, pp. 1045–1047, 1998.
[6] K. L. Wong and Y. F. Lin, "Circularly polarized microstrip antenna with a tuning stub," *Electron. Lett.*, vol. 34, pp. 831–832, 1998.

Acceleration of On-Surface MEI Method by New Metrons and FMM for 2-D Conducting Scattering

Y. W. Liu, Y. W. Zhao, and K. K. Mei

***Abstract*—In this paper, a new kind of metron is proposed and rapid integration provided by fast multipole methods (FMM) is implemented to dramatically reduce the CPU time of finding the MEI coefficients in the on-surface measured equation of invariance (OSMEI) method. The numerical example of the scattering of a large conducting elliptical cylinder shows that the computation speed is at least one order of magnitude faster than that of the original OSMEI, where sinusoidal metrons are used, and about 25% faster than that of the FMM, where the iteration method is used.**

***Index Terms*—Electromagnetic scattering, fast solvers.**

I. Introduction

The measured equation of invariance (MEI) method [1] has been developed to on-surface level (OSMEI) [2]–[4] to generate a sparse matrix with a minimum number of unknowns. Most of the time consumed by the MEI method is to find the matrix elements called MEI coefficients. Although the interpolation and extrapolation techniques [2], [5] can be used in reducing this burden for large object scattering, we still need to seek other possible solutions. Let us look at how many operations are needed for finding the MEI coefficients. In order to find the MEI coefficients in the OSMEI method, there are $2P$ integrations expressed in Section II should be completed, where P is the number of assumed surface currents, called metrons. For each integration, the operation count is of order $O(M^2)$, where M is the total number of unknowns. Therefore, the total operation count is $O(2PM^2)$. Usually, a set of sinusoidal functions is chosen as metrons. A few of the sinusoidal metrons is enough for small objects, but the number of sinusoidal metrons linearly increases with object size. This is the reason why finding the MEI coefficients is a dominant part for time consuming when the object becomes large. If a new kind of metron can be found to keep the number increasing slowly with the object size, it will bring great time saving. Furthermore, if the fast multipole methods (FMM), which reduces the operation count of the integration from $O(M^2)$ to $O(M^{1.5})$ [6], or $O(M^{1.33})$[7], or even $O(M \log M)$ [8], are used in the integration process in the OSMEI method, it would result in an extra time saving. In this paper, a new kind of metron is proposed and the FMM is used to accelerate the integration in the OSMEI method. Since far fewer new metrons are required for large objects and FMM is used to speed up the integration, the computation speed of the OSMEI is significantly increased. A numerical example shows that the computation speed is at least one order of magnitude faster than that of original OSMEI, where sinusoidal metrons are used, and is also about 25% faster than that of the FMM, where iteration is used.

II. Review of OSMEI Method

In order to understand how the metrons affect the integration, it is necessary to briefly review the OSMEI method. For simplicity, let us only consider TM scattering by a two-dimensional (2-D) perfectly conducting cylindrical scatterer whose axis is aligned with the z coordinate axis (Fig. 1). The scatterer has a boundary C with an arbitrary cross section. As described in [2] and [3], the MEI equations for each node under TM polarization can be written as

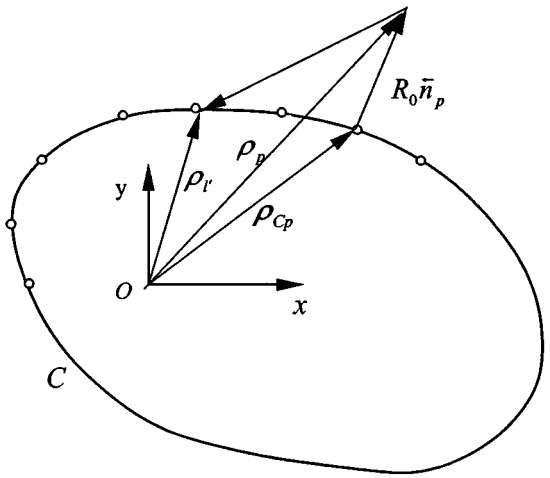

Fig. 1. A 2-D perfectly conducting cylinder with its new metron.

$$\sum_{n=1}^{N} a_n (H_l^s)_n^p + \sum_{n=1}^{N} b_n (E_z^s)_n^p = 0 \qquad p = 1, 2, \ldots, P \tag{1}$$

where N is the number of local nodes and a_n and b_n are known as MEI coefficients to be determined. If the circumference of the scatterer has a total of M nodes, there exist M MEI equations. $(H_l^s)^p$ and $(E_z^s)^p$ are known as measuring functions, with P pairs. The measuring functions $(H_l^s)^p$ and $(E_z^s)^p$ can be obtained by the following integrations:

$$[E_z^s(\rho)]^p = -\frac{\omega\mu_0}{4} \int_C J^p(\rho') H_0^{(2)}(k|\rho - \rho'|)\, dl' \tag{2}$$

$$[H_l^s(\rho)]^p = -\frac{1}{4j} \int_C J^p(\rho') \frac{\partial H_0^{(2)}(k|\rho - \rho'|)}{\partial n}\, dl' \tag{3}$$

where:

- ω angular frequency;
- μ_0 permeability of the free-space;
- j equal to $\sqrt{-1}$;
- P number of assumed surface currents, $J^p(\rho)$, which are known as metrons.

Usually, sinusoidal functions are chosen as metrons. Since only $(2N-1)$ coefficients in equation (1) are independent, P is required to be greater than or equal to $(2N-1)$. The number of integrations in (2) and (3) is equal to P. The coefficients a_n and b_n can be numerically found by substituting (2) and (3) into (1). Having applied the real metal boundary conditions of TM on the scatterer boundary C, we have the following system of equations:

$$[A]\underline{H_l^s} = [B]\underline{E_z^{\text{in}}} \tag{4}$$

where $[A]$ and $[B]$ are $M \times M$ cyclic band matrices with bandwidth N, where M is a large number (total nodes), and N is a small number (local nodes). Vector $\underline{E_z^{\text{in}}}$ represents incident electric field on the scatterer surface. Vector $\underline{H_l^s}$ stands for tangential scattered magnetic field components to be solved. Finally, the induced current density is a summation of the tangential scattered magnetic field and tangential incident magnetic field.

For 2-D scattering problems, N is a small number, say three, and is much less than M. What we want is to find a new kind of the metron that keeps N same and keeps the number of integrations required for

Manuscript received March 12, 1999; revised February 9, 2000. This work was supported in part by Hong Kong Research Grant Council CERG 9040273, 9040356, and 9040421.

The authors are with the Department of Electronic Engineering, City University of Hong Kong, Kowloon, Hong Kong.

Publisher Item Identifier S 0018-926X(00)07696-1.

finding the MEI coefficients in slowly increase with M rapidly increased to reduce the operation count.

III. New Metrons Plus FMM

In general, any orthogonal set of functions along the scatterer boundary C can be chosen as metrons. Usually, sinusoidal functions (or harmonic functions) are chosen as the metrons. As indicated in [2], the number of sinusoidal metrons is propotional to the electrical size of the scatterer, i.e.,

$$P = 2kR_{\max}\,\chi + 1 \qquad 0 \le l' \le L \tag{5}$$

where $R_{\max}$ is the radius of the smallest cylinder enclosing the scatterer and χ is a coefficient slightly larger than one. The fast Fourier transformation (FFT) is used to speed up the integration of (2) and (3) in [2], but the total number of operations still grows as $f^2 \log_2 f$ [2], where f is the frequency of the incidence wave. It is still time consuming for large object scattering. We need to find a new kind of metron to keep the number of metrons increasing slowly when the size is increased.

It is found that the following new metrons, as shown in Fig. 1, satisfy this requirement

$$J^p(l') = e^{-jkR_p}/R_p \qquad p = 1, 2, \ldots, P$$
$$P = 5 + \gamma\sqrt{kR_{\max}} \qquad 0.5 \le \gamma \le 0.7 \tag{6}$$

where

R_p $= |\rho_{l'} - \rho_p|$;
l' source position on the scatterer boundary C;
$\rho_{l'}$ corresponding position vector;

and

$$\rho_p = \rho_{Cp} + R_0\,\overleftarrow{n}_p \tag{7}$$

where:

ρ_{Cp} position vector distributed uniformly along the scatterer boundary C;
$\overleftarrow{n}_p$ outward-normal vector to the boundary C at ρ_{Cp};
R_0 constant.

Typical values of R_0 range from $R_{\max}/4$ to $R_{\max}/2$. The feature of the metrons in (6) is that both the phase and amplitude of the metrons are changed with the source positions. Because of this feature, in comparison with sinusoidal metrons, far fewer metrons are required for calculating the MEI coefficients. A possible reason for the metrons to greatly affect the integration is that using different metrons in OSMEI is equivalent to use different test functions in the MoM. Numerical experience tells us that the better metrons can keep the number of unknowns in each OSMEI equation almost same as the electrical size of the scatterer grows.

To further reduce the computation count of each integration in (2) and (3), a rapid integral algorithm based on the FMM [6], [7] is implemented as follows.

Assuming that ρ_i and $\rho_{i'}$ are the field point and source point, respectively, we have

$$\rho_{ii'} = \boldsymbol{\rho_i} - \rho_{i'} = \boldsymbol{\rho_i} - \rho_m + \rho_m - \rho_{m'} + \rho_{m'} - \boldsymbol{\rho_{i'}}$$
$$= \rho_{mm'} + (\rho_{im} - \rho_{i'm'}) \tag{8}$$

where ρ_m and $\rho_{m'}$ are the centers of the mth and m'th groups, which ρ_i and $\rho_{i'}$ belong to, respectively. Then, using the addition theorem of zero-order Hankel function of the second kind [9], (2) and (3) can be expressed as

$$[E_z^s(\rho_i)]^p \approx -\frac{\omega\mu_0}{8\pi}\Delta\phi \sum_{q=1}^{Q} V(\phi_q)T_{N_t}(\phi_q)e^{-j\boldsymbol{k}_q\cdot\rho_{im}} + [E_z^s(\rho_i)]^p_{\mathrm{M}} \tag{9}$$

$$[H_l^s(\rho_i)]^p \approx \frac{1}{8\pi}\Delta\phi \sum_{q=1}^{Q} \overleftarrow{n}_i \cdot \boldsymbol{k}_q V(\phi_q)T_{N_t}(\phi_q)e^{-j\boldsymbol{k}_q\cdot\rho_{im}} + [H_l^s(\rho_i)]^p_{\mathrm{M}}. \tag{10}$$

The first term in (9) and (10), which is calculated by the FMM, is the far interaction with all the nonnearby groups; the second term, which can be calculated by direct numerical computation similar to the MoM, is the contribution from the nearby groups. In (9) and (10), $\overleftarrow{n}_i$ is the outward-normal vector to the boundary C at ρ_i, $\Delta\phi = 2\pi/Q$, and $\phi_q = q\Delta\phi$, $q = 1, 2, \ldots, Q$, in which $Q/2 = k_oD + 5\ell n(k_oD + \pi)$ where D is the diameter of the circle enclosing the group, whereas $\boldsymbol{k}_q = k(\overleftarrow{x}\cos\phi_q + \overleftarrow{y}\sin\phi_q)$, $\overleftarrow{x}$ and $\overleftarrow{y}$ are the direction of the x- and y-axis, respectively, and

$$T_{N_t}(\phi) \approx \sum_{n=-N_t}^{N_t} H_n^{(2)}(k\rho_{mm'})e^{-jn(\phi-\varphi_{mm'}+\pi/2)} \tag{11}$$

$$V(\phi) = \int_C J^p(\rho_{i'})e^{j\boldsymbol{k}\cdot\rho_{i'm'}}\,dl' \tag{12}$$

where:

$\varphi_{mm'}$ angle between vector $\rho_{mm'}$ and x-axis;
$H_n^{(2)}$ n-order Hankel function of the second kind;
N_t $= Q/2$.

IV. Numerical Results

Using the new metrons in (6) and the FMM in the OSMEI method, the computational speed is significantly accelerated for the scattering of 2-D large conducting objects. Fig. 2 shows the comparison of the number of metrons required for the new metrons and sinusoidal metrons. It shows that the number of metrons can be reduced at least two orders of magnitude for the large object scattering. In Fig. 3, the comparison of the central processing unit (CPU) time as a function of the number of unknowns is plotted. It can be seen that the number of new metrons and the CPU time are dramatically reduced. The

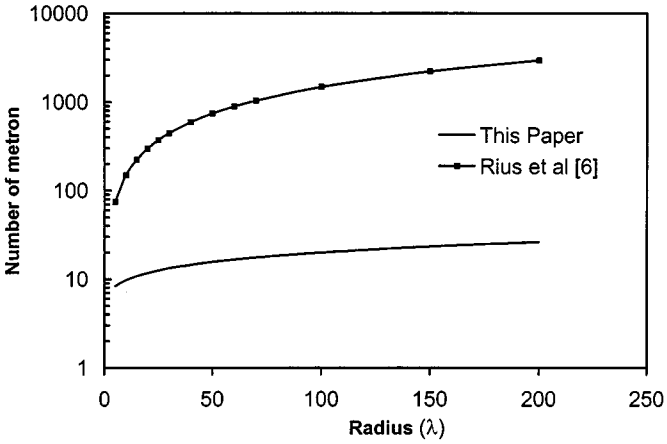

Fig. 2. Number of metron required in this paper is compared with that of Rius *et al.* [2].

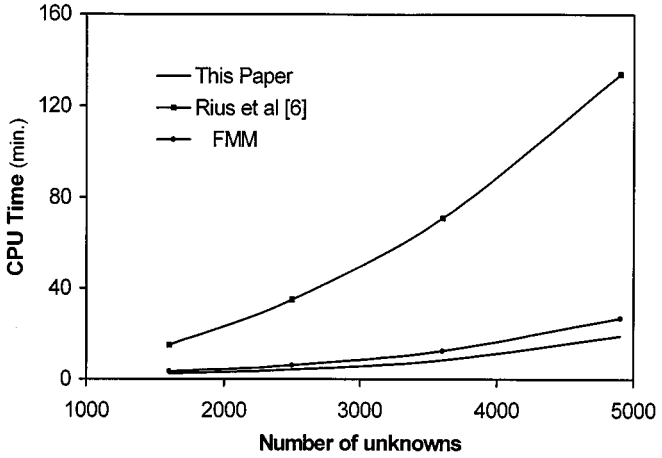

Fig. 3. CPU time of this paper is compared to Rius *et al.* [2] and FMM.

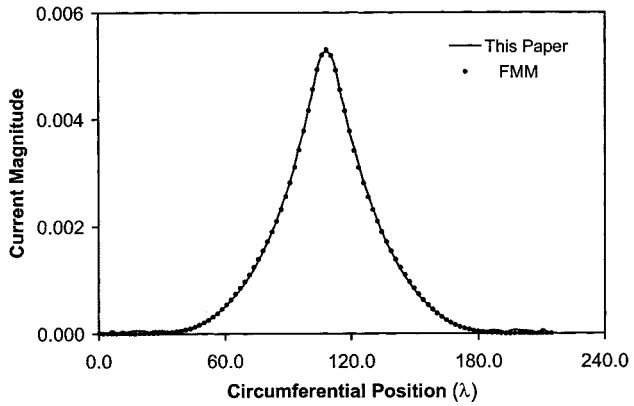

Fig. 4. Comparison of the current densities by the current approach and FMM for an elliptical cylinder illuminated by a 0° TM plane wave incidence. The major and minor semi-axis are $45\ \lambda$ and $22\ \lambda$, respectively.

CPU time for this new approach is about 25% less than that of the FMM with iteration method and about one order of magnitude less than that of the sinusoidal metrons with general integral methods. If an improved FMM version [8] is used, the CPU time can be further saved. Fig. 4 shows the comparison of the surface current densities by the current technique and the FMM for a large conducting elliptical cylinder with $45\ \lambda$ major semi-axis and $22\ \lambda$ minor semi-axis under 0° TM plane wave incidence. The agreement is very good. It should be emphasized that only the integration part rather than the iteration part of the FMM is used in the OSMEI method to accelerate the integration process.

V. Conclusion

A novel metron set for on-surface MEI (OSMEI) has been proposed. Far fewer metrons are required for calculating the MEI coefficients. The fast multipole procedure has been implemented to speed up the integration. The numerical examples show that the speed of the current approach is faster than that of the FMM with the iteration method. We hope that the new metrons can be extended to three-dimensional scattering problems.

References

[1] K. K. Mei, R. Pous, Z. Q. Chen, Y. W. Liu, and M. Prouty, "The measured equation of invariance: A new concept in field computation," *IEEE Trans. Antennas Propagat.*, vol. 42, pp. 202–214, Mar. 1994.

[2] J. M. Rius, R. Pous, and A. Cardama, "Integral formulation of the measured equation of invariance: A novel sparse matrix boundary element method," *IEEE Trans. Magn.*, vol. 32, pp. 962–967, May 1996.

[3] Y. W. Liu, K. K. MEI, and K. N. Yung, "Differential formulation of on-surface measured equation of invariance for 2-D conducting scattering," *IEEE Microwave Guided Wave Lett.*, vol. 8, pp. 99–101, Feb. 1998.

[4] H. Hirose *et al.*, "New integral formulation of the measured equation of invariance to analyze two dimensional cylinders with impedance boundary condition," in *IEEE Antennas Propagat. Soc. Int. Symp. Dig.*, Atlanta, GA, June 1998, pp. 1042–1045.

[5] Y. W. Liu, K. N. Yung, and K. K. Mei, "Interpolation, extrapolation and application of the measured equation of invariance to scattering by very large cylinders," *IEEE Trans. Antennas Propagat.*, vol. 45, pp. 1325–1331, Sept. 1997.

[6] V. Rokhlin, "Rapid solution of integral equations of scattering theory in two dimensions," *J. Computat. Phys.*, vol. 86, no. 2, pp. 414–439, 1990.

[7] R. L. Wagner and C. C. Chew, "A ray-propagation fast multipole algorithm," *Microwave Opt. Technol. Lett.*, vol. 7, no. 10, pp. 435–438, July 1994.

[8] J. M. Song, C. C. Lu, and W. C. Chew, "Multilevel fast multipole algorithm for electromagnetic scattering by large complex objects," *IEEE Trans. Antennas Propagat.*, vol. 45, pp. 1488–1493, Oct. 1997.

[9] N. Morita, N. Kumagai, and J. R. Mauts, *Integral Equation Methods for Electromagnetics*. Boston, MA: Artech House, 1990.

[10] M. Abramowitz and I. A. Stegun, *Handbook of Mathematical Functions*. New York: Dover, 1972.

Efficient Linear System Solution in Moment Methods Using Wavelet Expansions

L. Tarricone and F. Malucelli

***Abstract*—An efficient strategy is proposed to solve linear systems encountered when method of moments (MoM) and wavelet expansions are used. It exploits a high-performance matrix bandwidth reduction algorithm so that it can be taken advantage of direct banded solvers, which have a more favorable computational complexity with respect to the typically used iterative sparse methods. Speedups of up to seven have been experienced with respect to standard iterative sparse solvers.**

***Index Terms*—Electromagnetic scattering, method of moments (MoM), wavelet transform.**

I. Introduction

In the past few years, the use of wavelet expansions in the solution of electromagnetic problems has become more and more frequent. Wavelet expansions have been introduced, for instance, in conjunction with the method of moments (MoM) discretization of integral equations, in order to solve scattering problems with large-scale scatterers (thus, containing a variety of length scales with respect to wavelength)

Manuscript received April 8, 1999; revised December 8, 1999.

L. Tarricone is with the Dipartimento Ingeneria Elettronica e Informazione, 06131, Perugia, Italy (e-mail: tarricone@unipg.it).

F. Malucelli is with the Dipartimento Elettronica e Informazione, Politecnico di Milano, 20133 Milano, Italy.

Publisher Item Identifier S 0018-926X(00)07744-9.

TABLE I
PERFORMANCE OF SEVERAL BRA ALGORITHMS. MATRIX SIZE (N), INITIAL AND FINAL BANDWIDTH β, AND BANDWIDTH REDUCTION TIMES IN SECONDS ARE REPORTED FOR THREE DIFFERENT APPROACHES

		Final β			Times (s)		
N	In. β	CMK	TS	WBRA	CMK	TS	WBRA
72	60	42	38	24	0.05	1.4	0.06
162	147	31	40	16	0.27	7.9	0.24
246	230	54	170	21	0.69	14.8	0.51
503	491	62	294	41	2.9	138	1.6
870	852	77	Not avail.	49	19.3	Not conv.	2.1
1003	984	80	Not avail.	63	32.7	Not conv.	3.6

[1]–[5] or to analyze slot-apertures [6], microstrip floating line structures [7], as well as to study two-dimensional (2-D) and three-dimensional (3-D) dielectric structures [8], [9]. They have also been introduced in a boundary element method (BEM) to evaluate properties of multiconductor transmission lines in multilayered media [10] or to study scattering problems [11].

The above mentioned papers, which represent just a small and partial overview of the several possible applications, propose different uses of wavelet functions (as in these papers, both othonormal and semi-orthonormal spline wavelets are used [4], as well as multiresolution and compact-support functions [8], [9] or more standard local-support functions [Daubechies, Coiflets, etc.]).

Anyway, a common key issue for the majority of applications is the derivation of very sparse and well-conditioned linear systems, representing the numerical core of MoM approaches [8], [9], [12].

The moment matrix sparsity allows the use of very efficient iterative sparse solvers and the good condition number guarantees a low number of iterations to converge, with a consequent dramatic improvement of performance.

In this letter, we propose a method to make a further step in the enhancement of numerical performance. In fact, up to now, once the moment matrix has been sparsified using wavelet expansions, it has been assumed that iterative solvers are the best way to attack the linear system solution. We demonstrate here that by means of appropriate matrix transformations, the use of a banded direct solver outperforms the iterative approach, especially when nonsymmetric moment matrices are attained after split testing procedures in presence of compact-support functions [1], [2], [8], [9].

II. PROPOSED STRATEGY

The alternative strategy to iterative sparse solvers (ISS) is the use of a bandwidth reduction algorithm (BRA) in conjunction with a direct banded solver (DBS). The BRA evaluates a permutation matrix $\boldsymbol{P}$ (with $\boldsymbol{P}\boldsymbol{P}^{\boldsymbol{T}} = \boldsymbol{I}$) so that if we let

$$\underline{\boldsymbol{A}} = \boldsymbol{P}^{\boldsymbol{T}}\boldsymbol{A}\boldsymbol{P} \tag{1}$$

$\underline{\boldsymbol{A}}$ is a banded matrix, with small (hopefully minimum) bandwidth β. Therefore, if $\boldsymbol{P}$ is known, the original system $\boldsymbol{A}\boldsymbol{x} = \boldsymbol{B}$ can be transformed into

$$\underline{\boldsymbol{A}}\underline{\boldsymbol{x}} = \underline{\boldsymbol{B}} \tag{2}$$

with $\underline{\boldsymbol{x}} = \boldsymbol{P}^{\boldsymbol{T}}\boldsymbol{x}$, and $\underline{\boldsymbol{B}} = \boldsymbol{P}^{\boldsymbol{T}}\boldsymbol{B}$. System (2) is banded and can be solved with very efficient direct banded solvers [13], whose computational complexity depends quadratically on bandwidth β. This explains why the quality of the BRA, minimizing the sparse matrix bandwidth, plays a crucial role.

Several BRA have been proposed till now in the literature [13], but their performance was not attractive so that their use could have a substantial impact on the efficient solution of very sparse systems such those encountered in wavelet/MoM matrices. Moreover, all those methods were not able to deal with asymmetric matrices, which must be managed when compact-support wavelets are used [1], [2], [8], [9].

The authors have recently developed a new BRA, specifically devoted to handle MoM-like matrices, outperforming previous BRAs, and also able to solve both symmetric and nonsymmetric problems [14]. The approach [labeled herein as wonderful (W)BRA] is based on a matrix representation with an *adjacence graph* [13] and is an effective revisitation of an old-fashioned approach by Cuthill and McKee (CMK) [15]. WBRA has been discussed into details in [16] and the interested reader can also find fragments of code therein, implementing it. WBRA's performance are reported in Table I, where some results are given comparing it with respect to a commercial CMK implementation available in Matlab and a combinatorial iterative heuristics called tabu search (TS) [17]. In Table I the initial and final bandwidth (before and after minimization) is shown, as well as computational times to perform bandwidth reduction on an IBM 250T. Matrices are generated by using a MoM package for the analysis of microstrip circuits described in [12]. As apparent from Table I, the numerical complexity of WBRA is substantially lower. In fact, if we let N be the matrix dimension, and M the number of nonzero entries, WBRA needs $N^2M(\log N)$ operations in the worst case, whilst the other approaches need at least N^3M operations [16].

The efficiency of WBRA, as proved in Table I, reduces substantially the time needed to evaluate $\boldsymbol{P}$ and $\underline{\boldsymbol{A}}$, with a very small bandwidth for $\underline{\boldsymbol{A}}$. This means that the use of WBRA and DBS can now be outperforming with respect to the ISS strategy and this is proved in the following section.

III. RESULTS

We refer, for the proposed results, to a MoM discretization of a mixed-potential integral-equation formulation for the analysis of planar microstrip circuits, as described in [12]. The MoM matrices are transformed in accordance with the use of Battle–Lemarie multiresolution expansions as described in [1], [2], [8], [9], thus attaining nonsymmetric matrices when splitting and truncations are performed to comply with boundary conditions. A double-layer microstrip waveguide has been studied, with different basis expansions, and different threshold values v_t have been applied onto the moment matrices, so that values having magnitude less than v_t% of the largest entry are considered as zeros. Of course, different approximations are attained on varying v_t and errors have been estimated by comparing approximate results with the correct result attained without any thresholding. Different thresholds correspond to different matrix sparsities, as indicated in the second column of Tables II and III, where S is sparsity. Tables II and III resume

TABLE II
RESULTS FOR A MATRIX OF DIMENSION $N = 250$. COMPUTING TIMES (IN SECONDS) FOR WBRA+DBS STRATEGY VERSUS ISS STRATEGY ARE SHOWN, FOR DIFFERENT THRESHOLD VALUES, AND THE CORRESPONDING MATRIX SPARSITY S AND SOLUTION ERROR DUE TO THRESHOLDING EFFECTS. FOR ISS THE NUMBER OF ITERATIONS NEEDED TO CONVERGE IS SHOWN IN THE BRACKETS

v_t	S	Error	Solution Times (s) WBRA+DBS	ISS (Num. Iter.)
2%	99%	5.4%	0.08	0.09 (8)
1%	96%	2.4%	0.12	0.23 (17)
0.5%	91%	0.7%	0.21	0.48 (31)

TABLE III
RESULTS FOR A MATRIX OF DIMENSION $N = 478$. COMPUTING TIMES (IN SECONDS) FOR WBRA+DBS STRATEGY VERSUS ISS STRATEGY ARE SHOWN, FOR DIFFERENT THRESHOLD VALUES, AND THE CORRESPONDING MATRIX SPARSITY S AND SOLUTION ERROR DUE TO THRESHOLDING EFFECTS. FOR ISS THE NUMBER OF ITERATIONS NEEDED TO CONVERGE IS SHOWN IN THE BRACKETS

v_t	S	Error	Solution Times (s) WBRA+DBS	ISS (Num. Iter.)
2%	98%	4.8%	0.3	0.1 (11)
1%	94%	2.1%	0.64	1.4 (14)
0.5%	88%	0.6%	0.8	6 (28)

the results referred to two different cases of analysis of a double-layer microstrip, using different numbers of Battle–Lemarie wavelet functions. Different matrix sizes, $N = 250$ and $N = 478$, respectively, have been attained. Times are reported in seconds on an IBM 250 T using a DBS and an ISS from LAPACK suite, so that the same standard of performance is guaranteed for both solvers.

As apparent from Tables II and III, an appropriate value for thresholding is 0.5%, so that the approximation error is smaller than 1%. In this case, for $N = 250$, a speedup of nearly 2.3 is achieved, when using WBRA+DBS with respect to ISS, whilst for $N = 478$ a speedup of nearly 7.5 is observed.

If nonorthogonal wavelets are used, the condition number of the system matrix can be smaller than the one observed in the reported examples. In such cases, the number of iterations for an ISS can grow up substantially and the potential advantage of the proposed approach can be further increased.

IV. CONCLUSION

In this letter, it has been proved that the use of iterative sparse solvers is not the most efficient way to solve typical sparse linear systems encountered when multiresolution wavelet expansions are used in conjunction with the moment method discretization of integral equations. The use of a high-performance algorithm for sparse matrix bandwidth reduction, developed by the authors and suitable also for nonsymmetric cases, in fact, paves the way to the use of very efficient direct banded solvers, with a consequent dramatic improvement of performance. Solution times have been reduced up to a factor 7.5 with respect to the standard solution via iterative biconjugate gradient sparse solvers.

The strategy is general, and similar conclusions can be achieved when different wavelet functions are used combined with numerical approaches similar to MoM.

REFERENCES

[1] B. Z. Steinberg and Y. Leviathan, "On the use of wavelet expansions in the method of moments," *IEEE Trans. Antennas Propagat.*, vol. 41, pp. 610–619, May 1993.

[2] ——, "A multiresolution study of 2-D scattering by metallic cylinders," *IEEE Trans. Antennas Propagat.*, vol. 44, pp. 572–579, Apr. 1996.

[3] J. C. Goswami, A. K. Chan, and C. K. Chui, "On solving first-kind integral equations using wavelets on a bounded interval," *IEEE Trans. Antennas Propagat.*, vol. 43, pp. 614–622, June 1995.

[4] R. L. Wagner and W. C. Chew, "A study of wavelets for the solution of electromagnetic integral equations," *IEEE Trans. Antennas Propagat.*, vol. 43, pp. 802–810, Aug. 1995.

[5] G. Wang, "Analysis of EM scattering from conducting bodies of revolution using orthogonal wavelet expansions," *IEEE Trans. Electromagn. Compat.*, vol. 40, pp. 1–11, Feb. 1998.

[6] ——, "On the utilization of periodic wavelets expansions in the moment methods," *IEEE Trans. Microwave Theory Tech.*, vol. 43, pp. 2495–2497, Oct. 1995.

[7] G. Wang and G. Pan, "Full-wave analysis of microstrip floating line structures by wavelet expansion method," *IEEE Trans. Microwave Theory Tech.*, vol. 43, pp. 131–142, Jan. 1995.

[8] K. Sabet and L. P. B. Katehi, "Analysis of integrated millimeter-wave and submillimeter-wave waveguides using orthonormal wavelet expansions," *IEEE Trans. Microwave Theory Tech.*, vol. 42, pp. 2412–2422, Dec. 1994.

[9] ——, "An integral formulation of two- and three-dimensional dielectric structures using orthonormal multiresolution expansions," *Int. J. Num. Modeling*, vol. 11, pp. 3–19, 1998.

[10] G. Wang, G. Pan, and B. K. Gilbert, "A hybrid wavelet expansion and boundary element analysis for multiconductor transmission lines in multilayered dielectric media," *IEEE Trans. Microwave Theory Tech.*, vol. 43, pp. 664–675, Mar. 1995.

[11] G. Wang, "A hybrid wavelet expansion and boundary element analysis for EM scattering from conducting objects," *IEEE Trans. Antennas Propagat.*, vol. 43, pp. 170–178, Feb. 1995.

[12] A. Caproni, F. Cervelli, M. Mongiardo, L. Tarricone, and F. Malucelli, "Bandwidth reduced full-wave simulation of lossless and thin planar microstrip circuits," *J. Appl. Comput. Electromagn. Soc.*, vol. 13, no. 2, pp. 197–204, 1998.

[13] I. S. Duff, A. M. Erisman, and J. K. Reid, *Direct Methods for Sparse Matrices*. Oxford, U.K.: Oxford Univ. Press, 1986.

[14] A. Esposito, F. Malucelli, and L. Tarricone, "Bandwidth and profile reduction of sparse matrices: An experimental comparison of new heuristics," in *ALEX98*, R. Battiti and A. A. Bertossi, Eds. Trento, Italy, 1998.

[15] E. Cuthill and E. J. McKee, "Reducing the bandwidth of sparse symmetric matrices," in *Proc. ACM Nat. Conf.*, New York, Jan. 1969, pp. 157–172.

[16] A. Esposito, S. Fiorenzo Catalano, F. Malucelli, and L. Tarricone, "A new matrix bandwidth reduction algorithm," *Oper. Res. Lett.*, vol. 23, no. 3–5, pp. 99–107, 1999.

[17] M. Dionigi, A. Esposito, R. Sorrentino, and L. Tarricone, "A tabu search approach for an efficient solution of linear systems in electromagnetic problems," *Int. J. Numer. Modeling*, vol. 10, pp. 315–328, 1997.

A Physical Interpretation of the Equivalence Theorem

A. J. Booysen

***Abstract*—A physical interpretation of the equivalence theorem is presented. A simple example is used to show that the external and internal equivalence cases are analogous to incident, reflected, and transmitted wave problems in the geometrical optics sense.**

***Index Terms*—Equivalence theorem.**

I. Introduction

The aim of this letter is to present a better understanding of the mechanisms of the equivalence theorem [1, pp. 106–110]. This will be done by means of a simple scattering problem, namely that of an electromagnetic plane wave normally incident upon a planar dielectric interface. Consider first the general problem of sources $\overline{J}_1$ and $\overline{M}_1$ in medium (ϵ_1, μ_1), illuminating an object with constituent parameters (ϵ_2, μ_2), as depicted in Fig. 1(a). The equivalence theorem states that the equivalent current densities

$$\overline{J}_{s1} = \hat{n}_1 \times \overline{H}_1 \tag{1}$$

$$\overline{M}_{s1} = -\hat{n}_1 \times \overline{E}_1 \tag{2}$$

radiating in medium (ϵ_1, μ_1), together with the sources $\overline{J}_1$ and $\overline{M}_1$, will produce the true fields $\overline{E}_1$, $\overline{H}_1$ external to S, and null fields internal to S [Fig. 1(b)]. The currents densities $-\overline{J}_{s1}$ and $-\overline{M}_{s1}$, radiating in medium (ϵ_2, μ_2), will produce the true fields $\overline{E}_2$, $\overline{H}_2$ within S and null fields external to S [Fig. 1(c)]. The true electric field in region 1 can be expressed as

$$\overline{E}_1 = \overline{E}^i + \overline{E}\left(n = 1, \overline{J}_{s1}, \overline{M}_{s1}\right) \tag{3}$$

where for the two-dimensional (2-D) case [1, pp. 98–100, 228–230]

$$\overline{E}\left(n, \overline{J}_{s1}, \overline{M}_{s1}\right) = -\frac{k_n \eta_n}{4} \int_S \overline{J}_{s1} H_0^{(2)}(k_n r)\, dS + \frac{jk_n}{4} \int_S \overline{M}_{s1} \times \hat{r} H_1^{(2)}(k_n r)\, dS \tag{4}$$

and $k_n = 2\pi f \sqrt{\mu_n \epsilon_n}$, $\eta_n = \sqrt{\mu_n / \epsilon_n}$. The true electric field in region 2 (internal equivalence) is given by

$$\overline{E}_2 = \overline{E}\left(n = 2, -\overline{J}_{s1}, -\overline{M}_{s1}\right). \tag{5}$$

II. An Illustrative Example

Fig. 2 depicts a plane wave normally incident upon a planar dielectric interface. Following [1, p. 55], the total electric and magnetic fields can in the geometrical optics sense be expressed as

$$\overline{E}_{tot} = \overline{E}^i + \overline{E}^r \tag{6}$$

$$\overline{H}_{tot} = \overline{H}^i + \overline{H}^r \tag{7}$$

where

$$\overline{E}^i = e^{jk_1 x} \hat{z} \tag{8}$$

$$\overline{H}^i = \frac{1}{\eta_1} e^{jk_1 x} \hat{y} \tag{9}$$

Manuscript received May 7, 1999; revised November 29, 1999.

The author is with Grintek Antennas, Centurion 0046, Republic of South Africa.

Publisher Item Identifier S 0018-926X(00)07697-3.

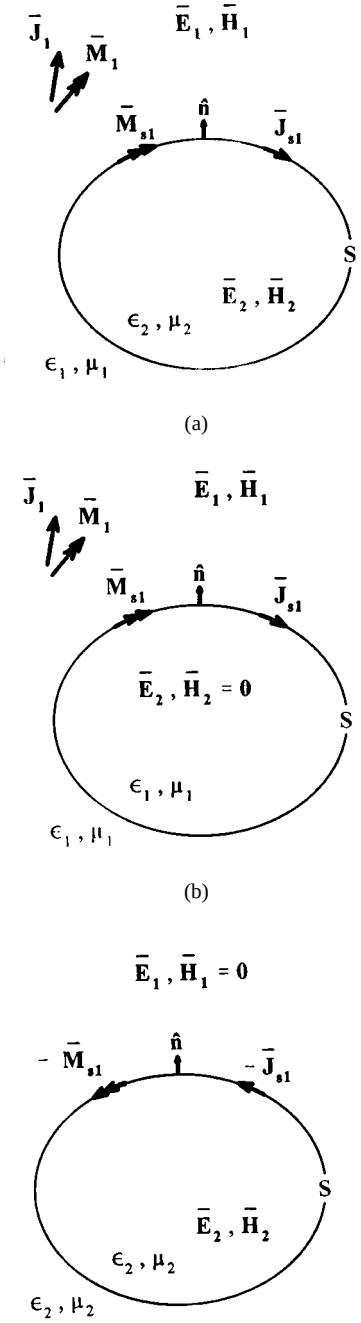

Fig. 1. Equivalence theorem.

$$\overline{E}^r = \Gamma e^{-jk_1 x} \hat{z} \tag{10}$$

$$\overline{H}^r = -\frac{\Gamma}{\eta_1} e^{-jk_1 x} \hat{y} \tag{11}$$

$$\Gamma = \frac{\eta_2 - \eta_1}{\eta_2 + \eta_1}. \tag{12}$$

The transmitted fields are given by

$$\overline{E}^t = (1 + \Gamma) e^{jk_2 x} \hat{z} \tag{13}$$

$$\overline{H}^t = \frac{1}{\eta_1}(1 - \Gamma) e^{jk_2 x}\, \hat{y} = \frac{1}{\eta_2}(1 + \Gamma) e^{jk_2 x} \hat{y}. \tag{14}$$

Employing the equivalence theorem, we let S enclose the dielectric interface by extending the upper and lower boundaries to infinity. On S we place surface current densities

$$\overline{\boldsymbol{J}}_{\boldsymbol{s1}} = \hat{\boldsymbol{n}}_{\boldsymbol{1}} \times \left(\overline{\boldsymbol{H}}_{\boldsymbol{1}} - \overline{\boldsymbol{H}}_{\boldsymbol{2}}\right) \tag{15}$$

$$\overline{\boldsymbol{M}}_{\boldsymbol{s1}} = -\hat{\boldsymbol{n}}_{\boldsymbol{1}} \times \left(\overline{\boldsymbol{E}}_{\boldsymbol{1}} - \overline{\boldsymbol{E}}_{\boldsymbol{2}}\right). \tag{16}$$

In the actual problem the tangential electric and magnetic fields must be continuous across the interface, resulting in $\boldsymbol{J}_{\boldsymbol{s1}} = \boldsymbol{0}$ and $\overline{\boldsymbol{M}}_{\boldsymbol{s1}} = \boldsymbol{0}$. If we now force $\overline{\boldsymbol{E}}_{\boldsymbol{2}}$ and $\overline{\boldsymbol{H}}_{\boldsymbol{2}}$ to be zero in accordance with Fig. 1(b), these current densities reduce to (1) and (2), respectively. For an observation point $(x,\ y = 0)$ as shown in Fig. 2, $S = (x' = 0,\ y')$, $dS = dy'$, and

$$\begin{aligned}\hat{\boldsymbol{r}} &= \frac{x - x'}{\sqrt{(x-x')^2 + (y-y')^2}}\hat{\boldsymbol{x}} + \frac{y - y'}{\sqrt{(x-x')^2 + (y-y')^2}}\hat{\boldsymbol{y}} \\ &= \frac{x}{\sqrt{x^2 + (-y')^2}}\hat{\boldsymbol{x}} - \frac{y'}{\sqrt{x^2 + (-y')^2}}\hat{\boldsymbol{y}} = r_x\hat{\boldsymbol{x}} + r_y\hat{\boldsymbol{y}}.\end{aligned} \tag{17}$$

Since the total fields at the interface are known, (1), (7), (9), and (11) yield

$$\overline{\boldsymbol{J}}_{\boldsymbol{s1}} = \frac{1}{\eta_1}(1 - \Gamma)\,\hat{z} = \frac{1}{\eta_2}(1 + \Gamma)\,\hat{z}. \tag{18}$$

Equations (2), (6), (8), and (10) similarly yield

$$\overline{\boldsymbol{M}}_{\boldsymbol{s1}} = (1 + \Gamma)\,\hat{\boldsymbol{y}}. \tag{19}$$

For external equivalence, these currents are substituted into (3), which must yield the true electric field in region 1. Note that since $\overline{\boldsymbol{E}}^{\boldsymbol{i}}$ is a plane wave normally incident upon a planar surface, $\overline{\boldsymbol{J}}_{\boldsymbol{s1}}$ and $\overline{\boldsymbol{M}}_{\boldsymbol{s1}}$ are constant on S and can thus be removed from under the integrals in (4). If we select the observation point x large enough so that $k_1 r \gg 1$, we can employ the large argument (asymptotic) forms of the Hankel functions [1, p. 463]

$$H_0^{(2)}(kr) \sim \sqrt{\frac{2j}{k\pi}}\frac{e^{-jkr}}{\sqrt{r}} \tag{20}$$

$$H_0^{(2)}(kr) \sim j\sqrt{\frac{2j}{k\pi}}\frac{e^{-jkr}}{\sqrt{r}}. \tag{21}$$

Substitution of (20), (21), (18), and (19) into (4) yields

$$\begin{aligned}\overline{\boldsymbol{E}}\left(n = 1,\ \overline{\boldsymbol{J}}_{\boldsymbol{s1}},\ \overline{\boldsymbol{M}}_{\boldsymbol{s1}}\right) = &-\sqrt{\frac{jk_1}{8\pi}}(1 - \Gamma)\hat{z}\int_S \frac{e^{-jk_1 r}}{\sqrt{r}}\,dS \\ &+ \sqrt{\frac{jk_1}{8\pi}}(1 + \Gamma)\hat{z}\int_S r_x\frac{e^{-jk_1 r}}{\sqrt{r}}\,dS.\end{aligned} \tag{22}$$

The integrals in (22) have the stationary phase (asymptotic) solutions [2]

$$\int_S \frac{e^{-jkr}}{\sqrt{r}}\,dS \sim \sqrt{\frac{2\pi}{k}}e^{-j(\pi/4)}e^{-jkr} \tag{23}$$

$$\int_S r_x\frac{e^{-jkr}}{\sqrt{r}}\,dS \sim \frac{x}{|x|}\sqrt{\frac{2\pi}{k}}e^{-j(\pi/4)}e^{-jkr}. \tag{24}$$

In region 1 of the external equivalence case $x > 0$, $r = x$ and $x/|x| = 1$. If (23) and (24) are substituted into (22), equation (10) results, i.e.,

$$\overline{\boldsymbol{E}}\left(n = 1,\ \overline{\boldsymbol{J}}_{\boldsymbol{s1}},\ \overline{\boldsymbol{M}}_{\boldsymbol{s1}}\right) = \Gamma e^{-jk_1 x}\hat{z} = \overline{\boldsymbol{E}}^{\boldsymbol{r}}. \tag{25}$$

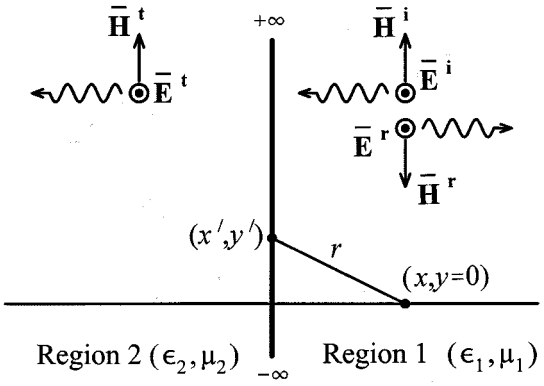

Fig. 2. Plane wave incident upon a planar dielectric interface

In other words, in the external case the radiated field represents the reflected field. The total field is given by the sum of the incident field and the reflected field. If we evaluate the integrals on the left-hand side (region 2) of the external equivalence case, $x < 0$, $r = -x$, and $x/|x| = -1$. Substitution of (23) and (24) into (22) now yields

$$\overline{\boldsymbol{E}}\left(n = 1,\ \overline{\boldsymbol{J}}_{\boldsymbol{s1}},\ \overline{\boldsymbol{M}}_{\boldsymbol{s1}}\right) = -e^{jk_1 x}\hat{z} = -\overline{\boldsymbol{E}}^{\boldsymbol{i}} \tag{26}$$

where $\overline{\boldsymbol{E}}^{\boldsymbol{i}}$ is given by (8). This result is to be expected, since the radiated field has to cancel the incident field in the null field region.

For the internal equivalence case, the total electric field in region 2 of Fig. 2 is given by (5). If we substitute equations (18) to (21) into (5), the result is

$$\begin{aligned}\overline{\boldsymbol{E}}\left(n = 2,\ -\overline{\boldsymbol{J}}_{\boldsymbol{s1}},\ -\overline{\boldsymbol{M}}_{\boldsymbol{s1}}\right) = &\sqrt{\frac{jk_2}{8\pi}}(1 + \Gamma)\hat{z}\int_S \frac{e^{-jk_2 r}}{\sqrt{r}}\,dS \\ &- \sqrt{\frac{jk_2}{8\pi}}(1 + \Gamma)\hat{z}\int_S r_x\frac{e^{-jk_2 r}}{\sqrt{r}}\,dS.\end{aligned} \tag{27}$$

The true field $\overline{\boldsymbol{E}}(n = 2,\ -\overline{\boldsymbol{J}}_{\boldsymbol{s1}},\ -\overline{\boldsymbol{M}}_{\boldsymbol{s1}})$ is evaluated on the left-hand side of the dielectric/air interface in Fig. 2, so that $x/|x| = -1$, $r = -x$ in (27). Substitution of (23) and (24) into (27) results in

$$\overline{\boldsymbol{E}}\left(n = 2,\ -\overline{\boldsymbol{J}}_{\boldsymbol{s1}},\ -\overline{\boldsymbol{M}}_{\boldsymbol{s1}}\right) = (1 + \Gamma)e^{jk_2 x}\hat{z} = \overline{\boldsymbol{E}}^{\boldsymbol{t}} \tag{28}$$

where $\overline{\boldsymbol{E}}^{\boldsymbol{t}}$ is given by (13). The radiated field thus represents the transmitted field in the case of an electromagnetically transparent object. In region 1 we have $x/|x| = 1$, which when substituted into (27) results in a null field, as expected.

III. Conclusion

By means of a very simple scattering example, it was shown that the mechanisms of the equivalence theorem can be directly related to more "physical" quantities in the form of the incident, reflected and transmitted fields. In the external equivalence case, the total field is given by the impressed (incident) field plus the scattered (reflected) field. The medium is that of region 1 in the original problem and by forcing the field in region 2 to be zero, we have conveniently created surface current densities which relate to the "external" problem only. In the internal case, there are no impressed fields and the radiated fields correspond to the transmitted fields. The medium is that of region 2 in the original problem. In this case the convenient selection of the fields in region 1 to be zero has allowed us to express the surface current densities in terms of the internal fields only.

REFERENCES

[1] R. F. Harrington, *Time-Harmonic Electromagnetic Fields*. New York: McGraw-Hill, 1961.

[2] L. B. Felsen and N. Marcuvitz, *Radiation and Scattering of Waves*. Englewood Cliffs, NJ: Prentice-Hall, 1973, pp. 386–387.

Single-Feed Dual-Band Planar Inverted-F Antenna with U-Shaped Slot

Pekka Salonen, Mikko Keskilammi, and Markku Kivikoski

***Abstract*—The development of small integrated antennas plays a significant role in the progress of rapidly expanding wireless communication applications. This paper describes a novel dual-band planar inverted-F antenna (PIFA) for wireless local area network applications. The proposed PIFA uses single feed only. A novel top-plate geometry, a U-shaped slot, is discussed. An example is given for this novel slot shape for frequency bands of 2.4 and 5.2 GHz. Simulation based upon method of moments (MoM) is used to model the performance of the antenna. Comparisons with results measured on fabricated antenna structures are provided for simulations validation.**

***Index Terms*—Antennas, dual-band antennas, handset antennas, printed antennas, slot antennas, wireless communications.**

I. INTRODUCTION

The rapid progress in wireless communications promises to make interactive voice, data, and video services available anytime and anyplace. Wireless communication systems come in a variety of different sizes ranging from small hand-held devices to wireless local area networks. The integration of different radio modules into the same piece of equipment has created a need for dual-band antennas.

Good results for dual-band operation have been achieved with planar inverted-F antennas (PIFA) for portable handsets, reported in [1]–[4]. In [1] a capacitively coupled load and feed method was studied in order to reduce the size of the PIFA. The dual-band operation was a major concern in [2]–[4]. Dual-band operation was achieved with parasitic inverted-L elements in [2] and with etched slots in the radiating element in [3] and [4]. The slot in the radiating element gives a more compact design for the antenna and, thus, space–volume is saved.

In this paper, we describe a new dual-band internal antenna for wireless communication systems. The basic idea is to combine the geometries used in [2]–[4] with single feed only. A design example of a dual-band PIFA which has a new U-shaped slot is given for frequencies of 2.4 and 5.2 GHz. This antenna is fabricated and the measured results are compared to simulations.

II. ANTENNA GEOMETRY

A new configuration of dual-band PIFA, having a U-shaped slot on the radiating patch is presented. The geometry is shown in Fig. 1 for the U-shaped slot. The length l and width w of the PIFA determines the lower resonant frequency, which can be approximated by the formula [4]

$$f_{l0} = \frac{c}{4(w+l)} \tag{1}$$

where

c	velocity of light;
l and w	length and width of the radiating element;
f_{l0}	lower operating frequency.

The upper resonant frequency for a U-shaped slot PIFA can be determined approximately from (1) in which length l and width w are replaced by l_2 and w_2, respectively, as shown in Fig. 1. For the upper frequency band (1) gives a slightly lower frequency value compared to simulations and experiment.

This dual-band antenna has almost the same size as a single-band planar inverted-F antenna operating at the lower frequency band. The radiating element was grounded by a shorting strip at its corner and fed near the shorting strip using coaxial cable. The antenna impedance can be easily matched to 50 Ω by controlling the feed position from the shorting strip.

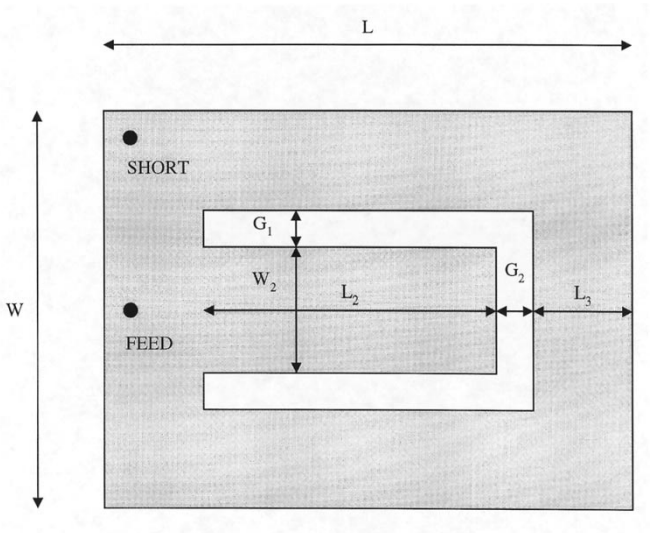

Fig. 1. Top-plate geometry configuration of single feed U-shaped slot dual-band PIFA.

TABLE I
TRENDS OF RESONANT FREQUENCY AND INPUT IMPEDANCE AS A FUNCTION OF THE GEOMETRICAL PARAMETERS OF THE U-SHAPED SLOT DUAL-BAND PIFA

	F1	F2	SWR1	SWR2
W, L ↑	↓			
L2 ↑		↓		
W2 ↑		↓		
G ↑		↓	↓	↓

III. PARAMETER STUDY

The sensitivity of resonant frequencies and input impedance to the geometry was studied for four parameters that were found to have the most critical influence. The values for the input impedance were specified as the frequency bandwidth in which the voltage standing wave ratio (VSWR) is less than 2 : 1. In this paper, the method of moments (MoM) has been used to allow modeling and simulation of the dual-band antenna.

Manuscript received July 7, 1999; revised February 9, 2000.

The authors are with the Institute of Electronics, Tampere University of Technology, 33101 Tampere, Finland.

Publisher Item Identifier S 0018-926X(00)07698-5.

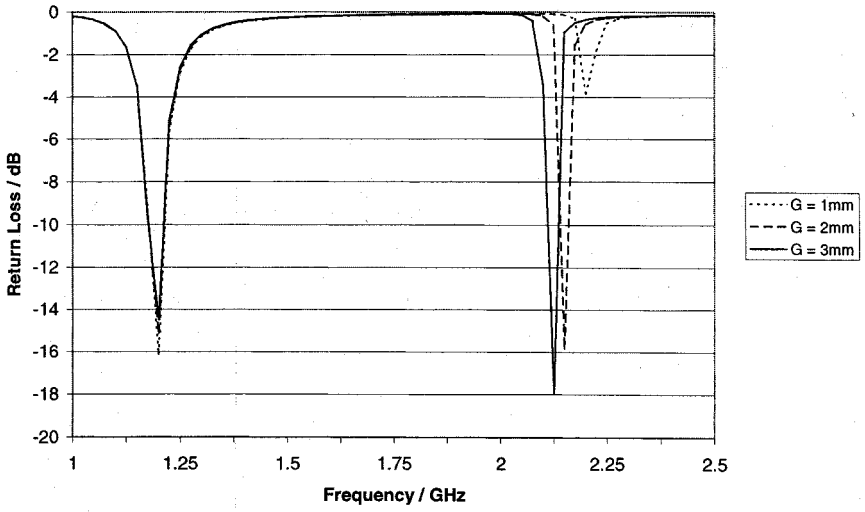

Fig. 2. Return loss of the U-shaped slot PIFA as a function of gap width in which $G1$ and $G2$ are equal length. Increase in $G1$ and $G2$ lowers the upper resonant frequency and null depth of the return loss. All other dimensions are fixed.

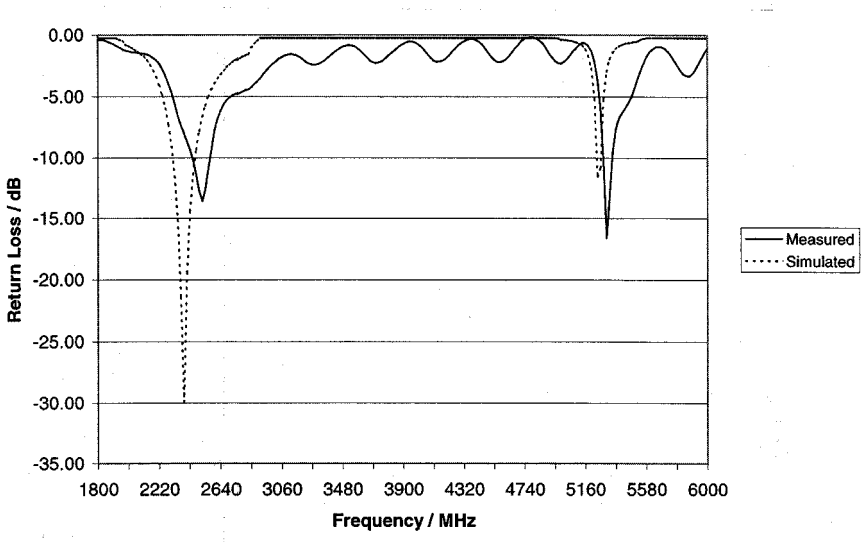

Fig. 3. Measured and simulated return loss.

The most critical parameters controlling the resonant frequencies of a dual-band U-shaped slot PIFA are summarized in Table I.

1) W—width of radiating element.
2) L—length of radiating element.
3) W_2—width of inner radiating element.
4) L_2—length of inner radiating element.

To understand the operation of our design we begin with a conventional PIFA (with the slot is removed) using air dielectric with dimensions $(l,\ w) = (40,\ 25)$ mm, height $h = 10$ mm in which a shorting strip of width $w_{\rm short} = 9$ mm is located at one end of the plate as shown in Fig. 1. The coax feed is connected directly to the top plate at the same edge as the shorting strip. The distance of the feed location in the middle of the top plate is also shown in Fig. 1. The resultant resonant frequency from the method of moments (MoM) simulations is 1.2 GHz, which agrees quite well with equation (1). To this conventional PIFA a U-shaped slot is added to determine its effects on the resonant frequencies and the bandwidth.

The dimensions of the slot are $L_2 = 27$ mm, $W_2 = 11$ mm, $L_3 = 8$ mm and $G = 2$ mm. The addition of the U-shaped slot had no effect on the lower resonant frequency and it remained at 1.2 GHz. The matching of the upper frequency can be controlled by the slot widths G_1 and G_2. The gap width G_2 is a compromise of input impedance because increase in G_2 tunes the lower frequency input impedance and mistunes the upper frequency input impedance, which as in Fig. 2. However, the best results in terms of input impedance matching are obtained when the gap widths G_1 and G_2 are equal.

This parameter study shows that for dual-band PIFA with U-shaped slot both frequencies can be determined independently. This makes the design procedure much simpler compared to dual-band PIFA with L-shaped slot.

IV. Experimental Validation

A dual-band antenna prototype was designed using U-shaped slot topology with the results in Section III for frequency bands 2.4 and 5.2 GHz. In order to characterize the antenna an HP8722D network analyzer was used to measure the input return loss of the antenna as a function of frequency.

The antenna was fabricated by etching the slot figure on a top plate, of 0.2-mm-thick copper and soldering it on a copper groundplane with a length of 180 mm and a width of 95 mm. The shorting strip dimensions were height 9 mm and width 3 mm. It should be emphasized here that the etching process was not accurate, which caused errors to the dimensions of the antenna. Thus, the 0.2-mm change in dimensions had the effect of altering the resonant frequencies. Also, the bandwidths of the antenna depend on the size and the shape of the groundplane, which is not optimized for these frequencies.

The dimensions for the U-shaped slot dual-band PIFA were $L = 15$ mm, $W = 12.5$ mm, $L_2 = 10.85$ mm, $W_2 = 4.2$ mm, G_1, $G_2 = 1.4$ mm and $L_3 = 1.25$ mm. The measured and simulated return loss of the U-shaped slot PIFA is shown in Fig. 3. The bandwidth of the lower resonant frequency is 230 MHz (9.6%), which agrees well with the simulations. However, the null depth is only half of that in the simulations because of the fabrication inaccuracies. The upper resonant frequency is slightly shifted up for the same reason. The null depth and the bandwidth 130 MHz (4%) agrees well with the simulations. This slot configuration is versatile for most wireless communication applications as for bandwidths. The lower frequency bandwidth is enough, e.g., for GSM or DCS, and the upper band is enough, e.g., for Bluetooth, which is not possible with L-shaped slot PIFA.

V. Conclusion

This letter focuses on the development of a dual-band planar inverted-F antenna using a novel top plate geometry. Series of simulations were used to investigate how different physical parts of the new U-shaped slot PIFA affect the input impedance, bandwidth, and resonant frequencies of the antenna. For the U-shaped slot PIFA both the lower and upper resonant frequency can be determined independently, which makes the design procedure simpler compared to L-shaped slot PIFA. The bandwidth of this antenna for the lower resonant frequency was 9.6% and for the upper resonant frequency bandwidth 4%. The wider bandwidth on the lower band of the U-shaped slot PIFA together with the easier design procedure makes it more versatile in wireless applications compared to L-shaped slot PIFA.

The results and design details on the antenna presented here can be used as starting points for engineers interested in utilizing low-profile dual-band planar inverted-F antennas in new wireless communications systems.

References

[1] C. R. Rowell and R. D. Murch, "A capacitively loaded PIFA for compact mobile telephone handsets," *IEEE Trans. Antennas Propagat.*, vol. 45, pp. 837–841, May 1997.

[2] K. L. Virga and Y. Rahmat-Samii, "Low profile enhanced-bandwidth PIFA antennas for wireless communications packaging," *IEEE Trans. Microwave Theory Tech.*, vol. 45, pp. 1879–1888, Oct. 1997.

[3] C. R. Rowell and R. D. Murch, "A compact PIFA suitable for dual-frequency 900/1800-MHz operation," *IEEE Trans. Antennas Propagat.*, vol. 46, pp. 596–598, Apr. 1998.

[4] Z. D. Liu, P. S. Hall, and D. Wake, "Dual-frequency planar inverted-F antenna," *IEEE Trans. Antennas Propagat.*, vol. 45, pp. 1451–1458, Oct. 1997.

Design of a Minimum-Loss Series-Fed Foldable Microstrip

C. G. Christodoulou, P. F. Wahid, M. Riad Mahbub, and M. C. Bailey

***Abstract*—The design and analysis of a series- fed, low-loss, inverted microstrip array antenna, operating at 1.413 GHz is presented. The array antenna is composed of two subarrays consisting of an equal number of microstrip patches connected together through a series microstrip line. The subarrays are coaxially fed 180° out of phase. This approach ensures a symmetric radiation pattern. The design approach for obtaining a low sidelobe ratio and a low loss microstrip array is accomplished using the IE3D code. Experimental and simulated data are presented and discussed.**

***Index Terms*—Microstrip arrays, spacecraft antennas.**

I. Introduction

One of the basic requirements of a radiometer antenna is to have very low radiation losses in order to maintain a desired radiometric resolution. In space applications, portability of the antenna is another requirement that must be satisfied. In this letter, these requirements are addressed through the design of a series-fed, foldable and inverted microstrip antenna array. This design minimizes the path length between the elements and, thus, minimizes ohmic losses [1], [2]. This reduction of losses makes the series configuration very attractive for radiometer applications. The inverted microstrip configuration is chosen because it provides less dispersion and dielectric losses than the conventional microstrip [3]. For the same characteristic impedance, substrate thickness, and for a comparable air gap, the attenuation due to conductor loss (usually the dominant loss mechanism) is improved by a factor of typically two to three [4]. The microstrip patches are supported by "*Rohacell*" foam material to reduce possible dielectric losses. The total antenna is composed of two subarray antennas, each consisting of an equal number of rectangular microstrip patch elements in series. The subarrays are fed 180° out of phase and an inverted ground plane is used to reduce radiation losses. This design yields low radiation losses and a radiation pattern with a narrow beamwidth and low sidelobes. A comparison between the measured and simulated data is presented and discussed.

II. Design Procedure

The first step is the determination of the dimensions of a single inverted microstrip patch. Next, additional patches are added to the array, one patch at a time to achieve the certain desired radiation pattern and input impedance. The inverted microstrip patch is the microstrip patch covered with dielectric layer and having the "*Rohacell*" foam as its dielectric substrate.

1) Calculation of the Patch Resonant Length: The resonant length of a single-patch microstrip antenna can be calculated from the empirical formula [5]

$$L = c \times (1 - 2V_R) \times (2 \cdot F_R \cdot \sqrt{\varepsilon_{eo}})^{-1} - 2 \cdot \Delta l \qquad (1)$$

Manuscript received August 27, 1999; revised May 2, 2000.

C. G. Christodoulou is with the Electrical and Computer Engineering Department, University of New Mexico, Albuquerque, NM 87131 USA.

P. F. Wahid is with the Electrical and Computer Engineering Department, University of Central Florida, Orlando, FL 32816 USA.

M. R. Mahbub is with Harris Corporation, Quincy, IL 62305 USA.

M.C. Bailey is with NASA Langley Research Center, Hampton, VA 23681 USA.

Publisher Item Identifier S 0018-926X(00)07699-7.

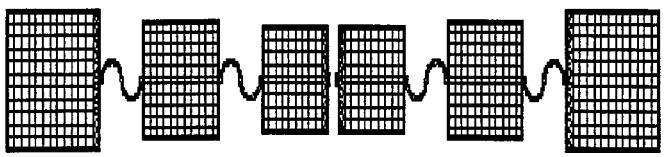

Fig. 1. The antenna with the two subarrays having three patches in each array.

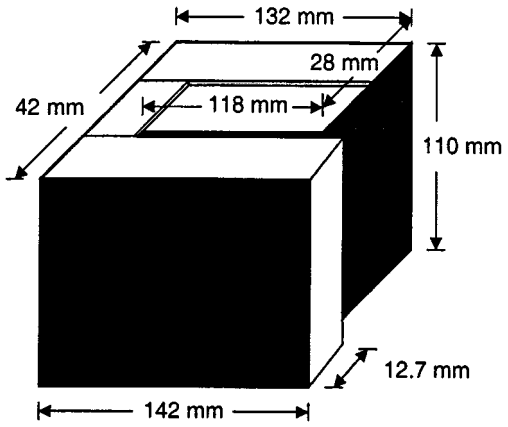

Fig. 2. Geometry of one foldable antenna (one half of the array). The ground plane is shown in its folding position.

where, Δl =capacitive cutback factor given by

$$\Delta l = 0.412H \times (\varepsilon_e + 0.3)(W/H - 0.2674) \times (\varepsilon_e - 0.258)^{-1}(W/H + 0.8)^{-1} \quad (2)$$

with c = speed of light, F_R = patch resonant frequency, ε_{eo} = effective dielectric constant of the patch without dielectric cover, ε_e = effective dielectric constant of the patch with dielectric cover, L = patch length, W = patch width, H = substrate thickness, and V_R =variation in resonant frequency. The optimum width of the microstrip antenna is given by

$$W = c \times (2 \cdot F_R)^{-1} \times [(\varepsilon_r + 1)/2]^{1/2}. \quad (3)$$

2) Calculation of the Effective Dielectric Constant: The effective dielectric constant of a dielectric covered patch antenna is given by [6]

$$\varepsilon_e = C_d/C_o \quad (4)$$

where C_o =capacitance/unit length without dielectric layer and C_d = capacitance/unit length with dielectric layer.

The capacitance per unit length of the dielectric-covered microstrip lines is

$$\frac{1}{C} = \frac{1}{4\pi\varepsilon_o}\int_0^\infty \left(1.6\frac{\sin(\beta W/2H)}{(\beta W/2H)} + 2.4(\beta W/2H)^{-2} \times \left[\cos(\beta W/2H) - \frac{2\sin(\beta W/2H)}{(\beta W/2H)} + \sin^2(\beta W/4H) \times (\beta W/4H)^{-2}\right]\right)^{-2} \times \left(\left[\varepsilon_{r1}\frac{\varepsilon_{r1} \times \tanh(\beta d/H) + 1}{\varepsilon_{r1} + \tanh(\beta d/H)} + \varepsilon_{r2}\coth(\beta)\right]\right)^{-1} d\beta \quad (5)$$

where

β Fourier transform variable;
ε_o permittivity of free space;
d height of the superstrate.

The integration in the last equation is performed twice—once to find C_d, the capacitance per unit length of dielectric covered antenna, and once to calculate C_o, the capacitance per unit length with no dielectric layer present.

3) Optimization of the Array Dimensions: Once the parameters of the single patch have been determined the array is assembled and optimized for best match in input impedance (for a uniform array design). The patches can be connected with straight, curved, or zigzagged inverted microstrip lines depending on the cross-polarization and sidelobe requirements. This particular array, designed for uniform excitation, yielded undesirable grating lobes when straight transmission lines were used. To reduce the size of grating lobes a curved microstrip line was used to make the connections between the patches. Thus, the physical distance between the patches was less than $\lambda_g/2$, but the actual electrical length was still $\lambda_g/2$ as shown in Fig. 1. This configuration yields a very small cross-polarized component (of the order of -30 dB) [5]. In this particular antenna, the substrate thickness of the inverted dielectric was 5 mil with a dielectric constant of 3.0. The "rohacell" thickness was 12.7 mm with a dielectric constant of 1.08. The patch dimensions were $L = 92$ mm, $W = 80.10$ mm, (first patch), $L = 103$ mm, $W = 87.10$ mm (second patch), and $L = 128$ mm, $W = 104.1$ mm (third patch). The distance of separation between patches was 58.7 mm with the first patch being fed by coaxial line.

4) Foldable Array Design: For convenient portability of this antenna it was designed to allow it to be folded at several locations along the array. The folds had to be designed without introducing any discontinuity in the inverted patch. The geometry of the foldable array is shown in Fig. 2. The ground plane was bent at specific locations by using thin metallic tape at those locations. The discontinuities in the ground plane were simulated as tiny perforations along the lines where the metallic tape was introduced.

III. Results

Using the IE3D simulator [6] both the unfolded and folded array configurations were simulated and compared to measured data. The input impedance of each of the foldable subarrays was 75.6 Ω and that of the unfolded subarrays was 66.0 Ω at a frequency of 1.413 GHz. The measured values of the input impedance were 59.12 Ω for the foldable arrays and 54.6 Ω for the unfolded arrays. The simulated return loss was calculated as -17 dB and the measured loss was -23.69 dB for the unfolded antenna. For the foldable antenna, the simulated and the measured return loss were -12.6 dB and -21.0 dB, respectively. The simulated and measured radiation patterns are shown in Figs. 3 and 4. Fig. 3 shows a comparison between the simulated and the measured patterns of the unfolded antenna shown in Fig. 2. Fig. 4 shows the effects of the frequency change on the radiation patterns of the foldable antenna.

IV. Conclusion

The design of a series fed microstrip array antenna using the IE3D simulator is presented and discussed. The optimization starts with the determination of the correct dimensions for one patch and then the building up of the array so that the input impedance is matched to a desired value. The patches dimensions are varied so as to obtain a certain sidelobe ratio and bandwidth. Care was taken in designing the distance of separation between adjacent patches in order to reduce any grating lobes. In the present design, curved microstrip lines are used to feed each adjacent element instead of a straight microstrip. The level of

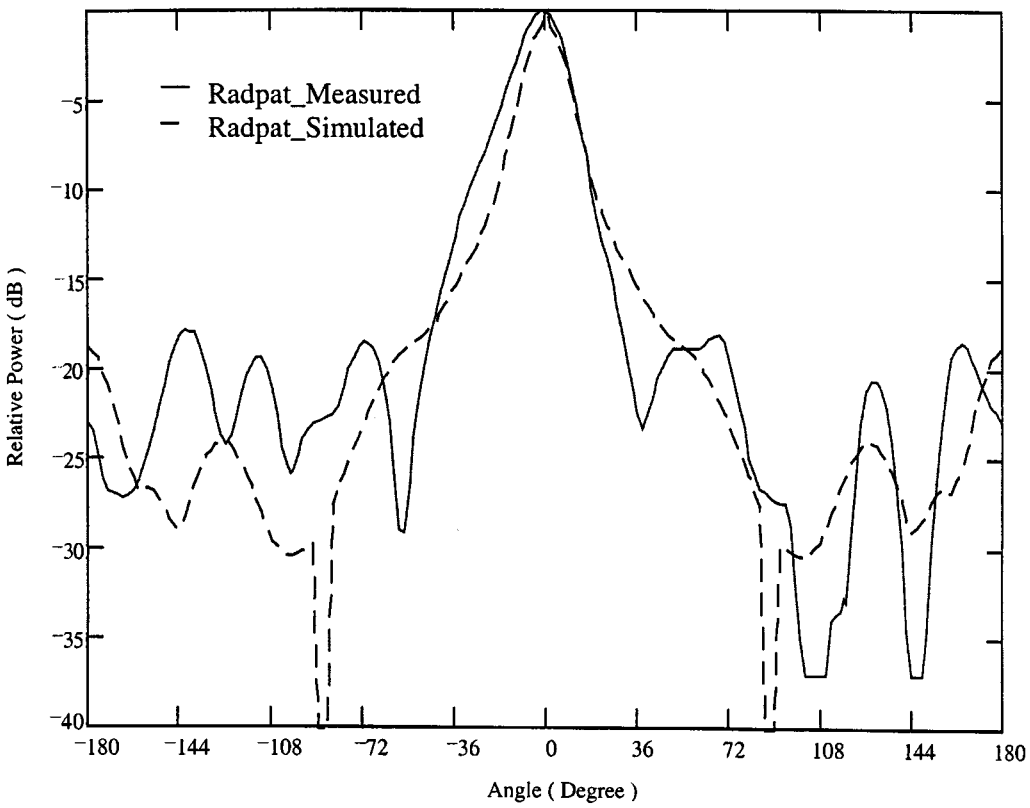

Fig. 3. Comparison of simulated and measured radiation pattern for the unfolded array at 1.413 GHz (E-plane cut).

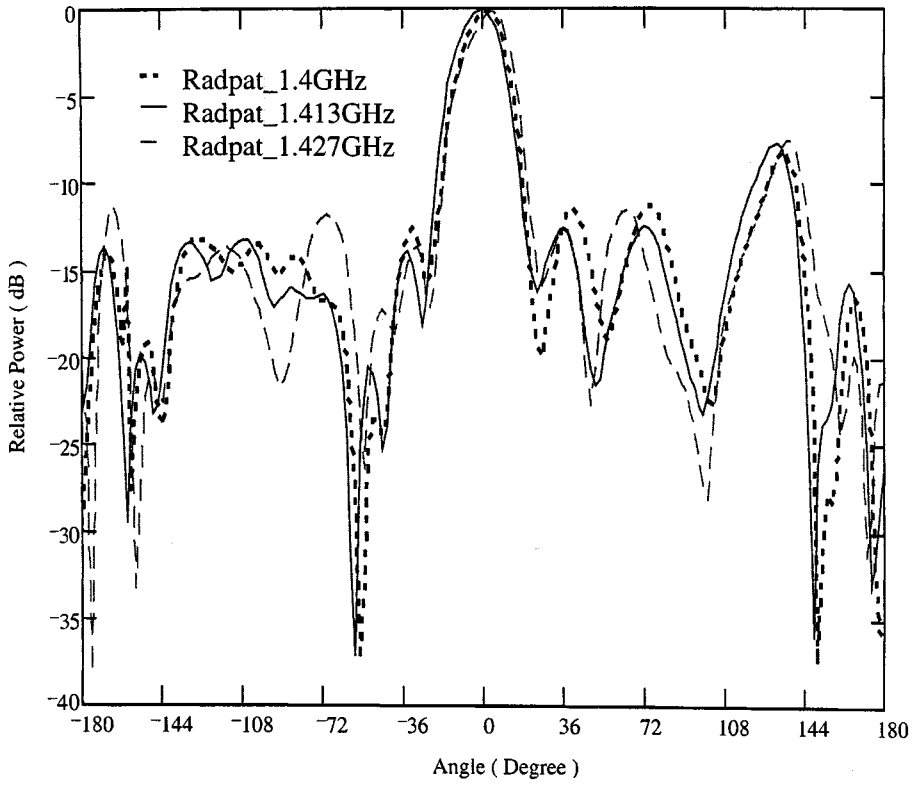

Fig. 4. Measured radiation pattern for the foldable array at different frequencies. (E-plane cut).

grating lobes diminishes significantly, without producing any significant level of cross polarization. The width of the connecting microstrip lines was also carefully chosen to limit the ohmic losses along the antenna and, thus, the total radiation losses.

REFERENCES

[1] T. Metzler, "Microstrip series arrays," *IEEE Trans. Antennas Propagat.*, vol. AP-29, pp. 174–178, Jan. 1981.

[2] K.-L. Wu, M. Spenuk, J. Litva, and D.-G. Fang, "Feed network effects on the radiation pattern of series-fed microstrip antenna arrays," *Proc. Inst. Elect. Eng.*, pt. H, vol. 138, no. 3, June 1991.

[3] J. M. Schellenberg, "CAD models for suspended and inverted microstrip," *IEEE Trans. Microwave Theory Tech.*, vol. 43, pp. 1247–1252, June 1995.

[4] G. P. Gauthier, A. Courtay, and G. M. Rebeiz, "Microstrip antennas on synthesized low dielectric-constant substrates," *IEEE Trans. Antennas Propagat.*, vol. 45, no. 8, pp. 1310–1314, Aug. 1997.

[5] R. Bancroft, "Accurate design of dual-band patch antennas," *Microwave RF*, vol. 27, pp. 113–118, Sept. 1988.

[6] Zeland Software Inc., "IE3D simulator,", Jan. 1997.

General Solution of a Monopole Loaded by a Dielectric Hemisphere for Efficient Computation

K. W. Leung

***Abstract*—A simple result for the general solution of a monopole loaded by a dielectric hemisphere is presented. The result can be calculated without the need for any numerical integration and, thus, it is computationally very efficient. In addition, the result is very easy to implement and should be useful to the design engineer.**

***Index Terms*—Dielectric antennas, monopole antennas.**

I. INTRODUCTION

In antenna designs, a dielectric loading can be added to change the antenna characteristics, such as the impedance, bandwidth, and radiation patterns [1]. It can also be used to provide insulation with the external medium [2]. There are many shapes of dielectric, but only the spherical one is convenient for an exact analysis [1], [2]. A rigorous solution of a monopole loaded by a dielectric hemisphere can be found in [3], where the exact Greens function was found analytically using the mode- matching method. In using the method of moments (MoM) to find the probe (or monopole) current [3], it is required to evaluate the quadruple integrals for the impedance matrix elements. Although the quadruple integrals can be reduced to double integrals by using the thin-wire approximation, considerable computation time and programming effort are still required to calculate the integrals numerically. In practice, the design engineer should prefer a simpler result that can be implemented easily and calculated quickly. Leung *et al.* [4] employed the single-mode theory to obtain a simple result for a probe along the axis of a dielectric hemisphere. The result, however, is not general and is only limited to frequencies around the TM_{101} mode of the dielectric hemisphere. In this letter, the general solution of a monopole along the axis of a dielectric hemisphere is presented. The result does not involve any numerical integration, and, thus, the computation is extremely fast. Furthermore, the expression is rather simple and can be implemented very easily. It is worth mentioning that for this particular configuration, all TE modes of the dielectric hemisphere vanish and only TM modes can be excited.

Manuscript received October 6, 1999; June 14, 2000. This work was supported by the Research Grant Council of the Hong Kong Special Administrative Region, China Project 9040433.

The author is with the Department of Electronic Engineering, City University of Hong Kong, Kowloon, Hong Kong (e-mail: eekleung@cityu.edu.hk).

Publisher Item Identifier S 0018-926X(00)07700-0.

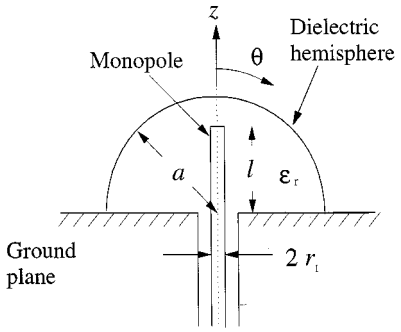

Fig. 1. Geometry of the monopole loaded by a dielectric hemisphere.

II. THEORY

The configuration is shown in Fig. 1. A monopole of length l and radius r_1 is located at the center of a dielectric hemisphere of radius a and dielectric constant ε_r. In the following formulation, z and z' refer to the field and source coordinates, respectively. To begin with, image theory is used to obtain the equivalent problem of a dipole embedded inside a dielectric sphere. Denote $G(z, z')$ as the Green's function for the z-directed E-field due to a point current along the z-axis. Using the result of [3], we have, for a thin monopole ($r_1 \ll l$ and $kr_1 \ll 1$)

$$G(z, z') = \frac{-j}{\omega\varepsilon}\left(\frac{\partial^2}{\partial z^2} + k^2\right)\frac{e^{-jkR}}{4\pi R} - \frac{1}{4\pi\omega\varepsilon k} \cdot \frac{1}{z^2 z'^2}\sum_{n=1}^{\infty} n(n+1)(2n+1)\alpha_n^{\mathrm{TM}}\hat{J}_n(kz')\hat{J}_n(kz) \tag{1}$$

where

$$\alpha_n^{\mathrm{TM}} = \frac{-\lfloor \hat{H}_n^{(2)\prime}(ka)\hat{H}_n^{(2)}(k_0a) - \sqrt{\varepsilon_r}\hat{H}_n^{(2)}(ka)\hat{H}_n^{(2)\prime}(k_0a)\rfloor}{\hat{J}_n{}'(ka)\hat{H}_n^{(2)}(k_0a) - \sqrt{\varepsilon_r}\hat{J}_n(ka)\hat{H}_n^{(2)\prime}(k_0a)} \tag{2}$$

is the reflection coefficient at the DR boundary, $R = \sqrt{r_1^2 + (z-z')^2}$, and $k = \sqrt{\varepsilon_r}k_0$. In (1) and (2), $\hat{J}_n(x)$ and $\hat{H}_n^{(2)}(x)$ are the Schelkunoff-type [3] spherical Bessel function of the first kind and Hankel function of the second kind, respectively, both of them of order n. By enforcing the boundary condition that the total E-field vanishes on the (equivalent) dipole surface, an integral equation for the dipole current is obtained. The MoM with the Galerkin's procedure is used to solve the dipole current. The current is first expanded as $I(z) = \sum_{q=1}^{N} I_q f_q(z)$, where $f_q(z)$ is a piecewise sinusoidal (PWS) function given by $f_q(z) = [\sin k(d - |z - z_q|)]/\sin kd$ for $|z - z_q| < d$ and $f_q(z) = 0$ otherwise, with $z_q = -l + qd$ and $d = 2l/(N+1)$. The unknown expansion coefficients I_q's are solved via the matrix equation $[Z_{pq}^P + Z_{pq}^H][I_q] = [f_p(0)]$, where Z_{pq}^P and Z_{pq}^H are the impedance integrals associated with the first term (particular solution) and second term (homogeneous solution) of (1), respectively. The efficient evaluation of the impedance integrals Z_{pq}^P was discussed in

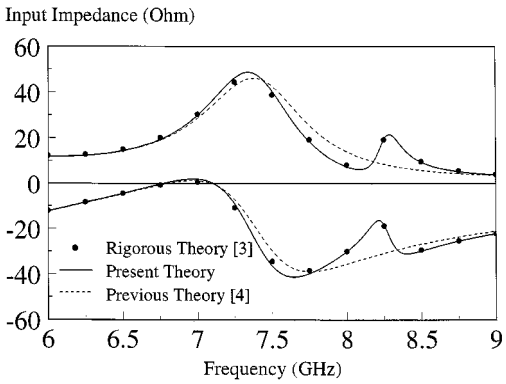

Fig. 2. Comparison of the present, rigorous, and previous simplified theories: $a = 12.5$ mm, $\varepsilon_r = 9.5$, $l = 5.0$ mm, $r_1 = 0.63$ mm, and $N = 5$.

[5] and is not duplicated here. Instead, we will concentrate on the Z_{pq}^H integral, which can be written as

$$Z_{pq}^H = \frac{1}{4\pi\omega\varepsilon k}\sum_{n=1}^{\infty} n(n+1)(2n+1)\alpha_n^{\mathrm{TM}}\Lambda_n(p)\Lambda_n(q) \tag{3}$$

where, for $i = p,\ q$

$$\Lambda_n(i) = \int_{z_{i-1}}^{z_{i+1}} \frac{\hat{J}_n(kz)}{z^2}\cdot\frac{\sin k(d-|z-z_i|)}{\sin kd}\,dz. \tag{4}$$

To evaluate $\Lambda_n(i)$ analytically, the absolute sign of the PWS function is first removed by breaking (4) into two integrals. Next we apply the identity $\sin k[(d \pm z_i) \mp z] = \sin k(d \pm z_i)\cos kz \mp \cos k(d \pm z_i)\sin kz$ to the integrals. Then the crucial step is to integrate $[\hat{J}_n(kz)/z^2]\cos kz$ and $[\hat{J}_n(kz)/z^2]\sin kz$. To do this, we first note that $\cos\ kz$ and $\sin\ kz$ can be alternatively written as $-\hat{Y}_0(kz)$ and $\hat{J}_0(kz)$, respectively. Then based on an integral formula for a product of two cylindrical Bessel functions $A_\mu(t),\ B_\nu(t)$ [6], the following integral was derived:

$$\begin{aligned}\int^z \frac{\hat{A}_n(t)\hat{B}_m(t)}{t^2}\,dt &= \frac{1}{(n+m+1)(n-m)}\\ &\cdot\left\{\frac{n-m}{z}\hat{A}_n(z)\hat{B}_m(z)\right.\\ &\left.-\left[\hat{A}_{n+1}(z)\hat{B}_m(z)-\hat{A}_n(z)\hat{B}_{m+1}(z)\right]\right\}\end{aligned} \tag{5}$$

where $\hat{A}_n(t) = \sqrt{\pi t/2}A_{n+(1/2)}(t)$ and $\hat{B}_m(t) = \sqrt{\pi t/2}\ B_{m+(1/2)}(t)$ denote any two Schelkunoff-type spherical Bessel/Hankel functions and $n \neq m$. Since the order of $\hat{J}_n(kz)$ in $G(z, z')$ starts from $n = 1$, it is always unequal to those of $\hat{Y}_0(kz)$ and $\hat{J}_0(kz)$. Therefore, the condition that $n \neq m$ in (5) is satisfied in the present problem. After tedious manipulation, the result of Z_{pq}^H is found to be surprisingly simple

$$Z_{pq}^H = \frac{k}{4\pi\omega\varepsilon}\cdot\frac{1}{\sin^2 kd}\sum_{n=1}^{\infty}\frac{2n+1}{n(n+1)}\alpha_n^{\mathrm{TM}}L_n(p)L_n(q) \tag{6}$$

where, for $i = p,\ q$

$$L_n(i) = \sum_{j=-1}^{1} A(j)\hat{J}_n(ku_{ij}) \tag{7}$$

with $u_{ij} = -l + (i+j)d$, $A(\pm 1) = 1$, and $A(0) = -2\cos kd$. It can be proved that the result of [4] is only the $n = 1$ term of (6). Note that Z_{pq}^H now does not involve any integration and, thus, the calculation is extremely fast. Moreover, implementation of (6) is very easy. The only care that has to be exercised is that u_{ij} may be zero for some $i,\ j$, at which $\hat{J}_n(ku_{ij}) = 0$. Therefore, u_{ij} should be checked in the program, as the (backward) recurrence formula for $\hat{J}_n(x)$ cannot be used when $x = 0$. Now the overall solution is computationally very efficient, as the other impedance integral, Z_{pq}^P, can also be calculated without the need for any numerical integration [5]. After I_q's are found, the input impedance can be obtained by simply using $Z_{\mathrm{in}} = \beta\sum_{n=1}^{N} I_n f_n(0)$, where $\beta = 1$ for the equivalent dipole configuration and 1/2 for the original (monopole) configuration.

III. Results

In this letter, five current expansion modes ($N = 5$) were used in the calculations. Fig. 2 compares the present theory with the rigorous solution [3] and the previous simplified theory [4]. It is seen that excellent agreement between the present and rigorous solutions is obtained over the whole frequency band. In contrast, the previous simplified theory is valid only in the low-frequency portion, as expected. The programs were run on a SunSPARC 20 Model 612 workstation. It was found that for the present theory the average computation time for a frequency point was only 1 ms, whereas it took a few seconds for the rigorous theory. Other values of l, ε_r, and a were used and, in all cases, the present theory was in excellent agreement with the rigorous theory. The results, however, are omitted here for brevity.

References

[1] J. E. Wheeler and R. D. Nevels, "Reflection and transmission properties of annular slot covered by dielectric hemisphere," *Proc. Inst. Elect. Eng.*, pt. H, vol. 136, pp. 59–63, Feb. 1989.

[2] R. W. P. King and G. S. Smith, *Antennas in Matter*. Cambridge, MA: MIT Press, 1981, ch. 10.

[3] K. W. Leung, K. M. Luk, K. Y. A. Lai, and D. Lin, "Theory and experiment of a coaxial probe fed dielectric resonator antenna," *IEEE Trans. Antennas Propagat.*, vol. 41, pp. 1390–1398, Oct. 1993.

[4] K. W. Leung, K. W. Ng, K. M. Luk, and E. K. N. Yung, "Simple formula for analyzing the center-fed hemispherical dielectric resonator antenna," *Electron. Lett.*, vol. 33, pp. 440–441, Mar. 1997.

[5] R. C. Hansen, "Formulation of echelon dipole mutual impedance for computer," *IEEE Trans. Antennas Propagat.*, vol. AP-20, pp. 780–781, Nov. 1972.

[6] G. N. Watson, *A Treatise on the Theory of Bessel Functions*, 2nd ed. Cambridge, U.K.: Cambridge Univ. Press, 1944, p. 134.

Building Material Characterization from Complex Transmissivity Measurements at 5.8 GHz

Iñigo Cuiñas and Manuel García Sánchez

***Abstract*—In this letter, an improvement of the well-known internal multireflection model of transmission coefficients is proposed in order to obtain better agreement with complex measured data. The reason for the introduced changes is explained. To obtain the data, measurements were performed at 5.8 GHz using a vector network analyzer, which provided information on the amplitude and phase of the transmission coefficient. By comparing the model and measurements, both the real and imaginary parts of the material complex permittivity were estimated for four different building materials.**

***Index Terms*—Dielectric materials, electromagnetic scattering, permittivity measurement, urban propagation.**

I. Introduction

Wireless local area networks are expanding rapidly as a result of the increasing demand on computer communications and the advances on digital radio systems. Several frequency bands have been proposed for use by these systems, including the 160-MHz band centered at a frequency of 5.8 GHz [1], which is considered in this paper. Radio planning tools are usually employed to plan the deployment of these networks. The accuracy of these tools depends on the availability of good electromagnetic models of the obstacles in the environment at the frequency of operation. The validation of the models requires measurement data on radiowave propagation through building materials. The internal multireflection model [2] has been widely used for this purpose during recent years, but it has been only compared to amplitude measurements.

The measurement system used to obtain the results presented in this paper is based on the "free-space" technique [3]–[5] that provides information on amplitude and phase of the transmission coefficient.

A correction of the internal multireflection model is proposed in order to deal with the phase of the transmission coefficients. The modified model is then compared with the results of measurements at 5.8 GHz.

II. Measurement Setup

As described in [3]–[5], the measurement system consists of a vector network analyzer (VNA), an HP-8510-C, which can perform S-parameter measurements of a quadripole connected between its two ports, from 45 MHz up to 50 GHz. This capability is used by the system to obtain the frequency response of the radio channel by connecting two identical standard 20-dBi pyramidal horns to ports 1 and 2 through flexible microwave coaxial cables (Fig. 1). Measuring the S_{21} parameter of such quadripole the frequency response of radio channel is obtained over a 160-MHz bandwidth at 5.8 GHz. To reduce the effect of the thermal noise on the measurement, the averaging factor of the VNA is set to ten.

A calibration was first performed without any obstacle between the antennas, to measure the effect of cables, amplifier, antennas and free-space propagation. Then, the material slab to be measured was placed vertically between both antennas and the measurement was repeated. The attenuation due to the obstacle as a function of frequency is obtained by comparing both measurements.

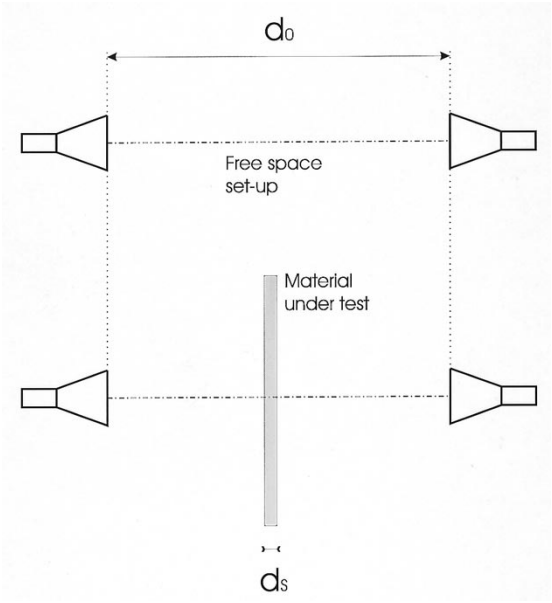

Fig. 1. Measurement system setup.

In order to ensure that the incident and transmitted waves could be approximated as plane waves the antennas were placed 5 m apart, which is larger than twice the far field distance. The directivity of the antennas was enough to guarantee that just the direct signal through the material was being measured and any multipath due to any other scatterer present in the environment was filtered out. This was verified by obtaining the impulse response of each measurement through an inverse fast Fourier transform (FFT) and checking that just the direct component was present [6].

Following a similar process to that described in [3], the error in the measurement was estimated to be between ± 0.035 dB for the amplitude and $\pm 0.7^{\circ}$ for the phase of the transmission coefficient.

Four different types of materials were measured. Three of them, a 2.5-m $\times$ 1.4-m $\times$ 5-mm crystal glass, a 2.5-m $\times$ 1-m $\times$ 10-mm slab of chipwood, and a 2.6-m $\times$ 1.2-m $\times$ 10-mm plasterboard panel, were made of a single layer and did not exhibit any oriented structure. However, the brick wall, sized 7 m $\times$ 3 m $\times$ 105 mm was made of 25-cm $\times$ 10-cm $\times$ 7-cm bricks that had an oriented internal structure of air holes and were laid horizontally. The sample sizes were large enough to ensure that the 3-dB illuminated area, an ellipse with a major axis of 80 cm, falls within the limits of the slabs, thus reducing any diffraction effects on the edges of the samples.

III. Extended Multireflection Model

Since the transmission coefficient value is related to the electromagnetic characteristics of the obstacle, the fit of a transmission model to measured data leads to a good estimation of the electromagnetic characteristics of the obstacle in the frequency band of interest.

The classical multireflection model for the transmission coefficients takes into account both the incident field that crosses the obstacle directly, and other components that reach the opposite side of it, after being internally reflected between both interfaces [7]. The resulting

Manuscript received October 26, 1999; revised April 1, 2000. This work was supported by Spanish CICYT, Project TIC97-1129-C04-03.

The authors are with the Department Tecnoloxías das Comunicacións, Campus Universitario s/n, Universidade de Vigo, E36200 Vigo, Spain.

Publisher Item Identifier S 0018-926X(00)07701-2.

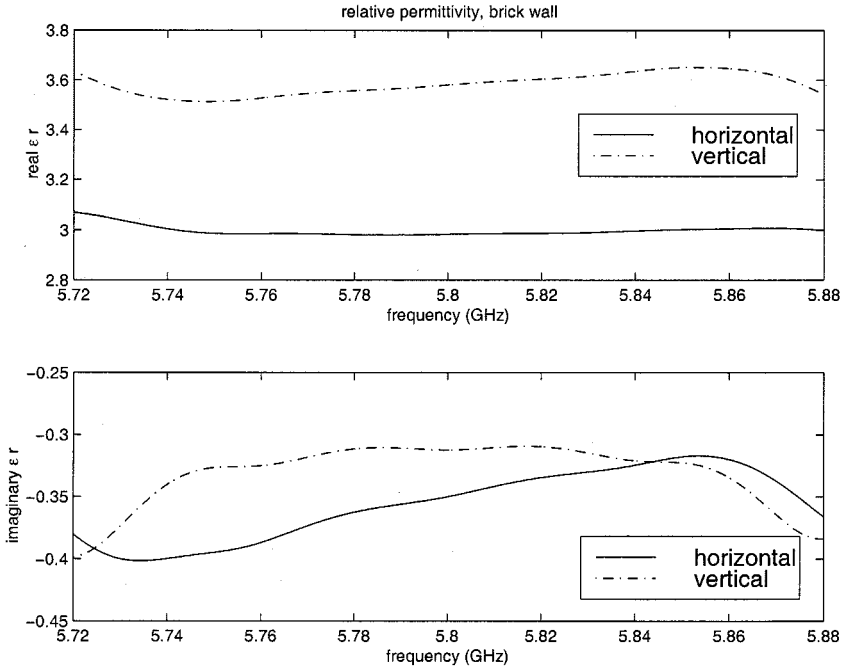

(a)

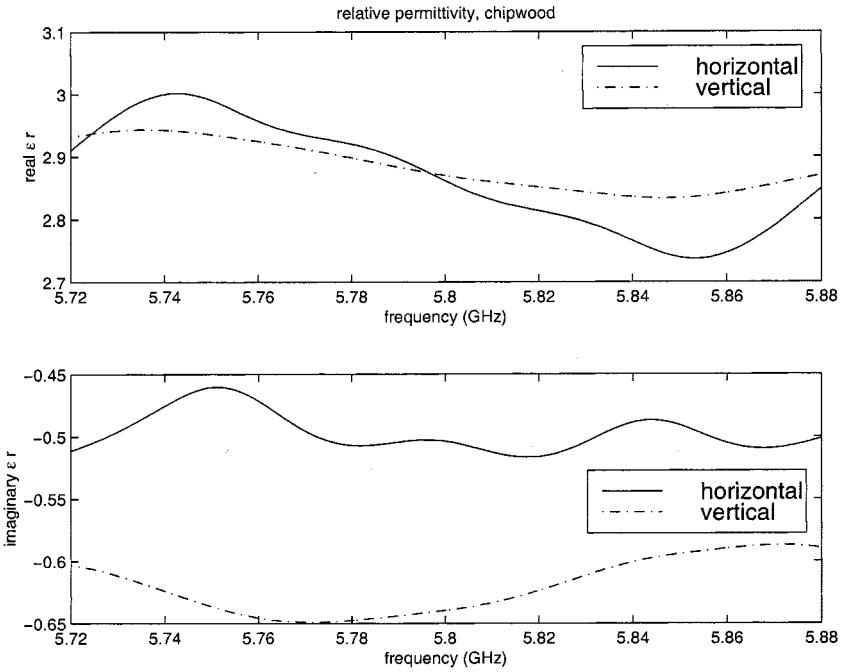

(b)

Fig. 2. Frequency and polarization dependence of the dielectric constant. (a) Brick wall. (b) Chipwood slab.

transmission coefficient for normal incidence (or, as it is known, transmissivity), is classically enunciated, as in (1)

$$T_s = \frac{(1-\Gamma^2)e^{-j\cdot k_S\cdot d_S}e^{-\alpha\cdot d_S}}{(1-\Gamma^2 e^{-j\cdot 2\cdot k_S\cdot d_S}e^{-2\cdot\alpha\cdot d_S})} \tag{1}$$

where

k_S propagation constant across the obstacle;

α attenuation constant of the obstacle;

d_S thickness of the obstacle;

Γ Fresnel reflection coefficient at the interface of free-space and the material under test.

The numerator in (1) contains the information on the transmission of the electric field across the obstacle, while the denominator is devoted to the sum of the field components originating from the multireflection inside the slab. This is depicted in Fig. 1.

TABLE I
ELECTROMAGNETIC CHARACTERIZATION. (a) HORIZONTAL POLARIZATION. (b) VERTICAL POLARIZATION

Material	Re{ε_r}	Im{ε_r}	tan(δ)	σ (S/m)
Glass	5.98	-1.08	0.18	0.36
Chipwood	2.87	-0.50	0.17	0.16
Plasterboard	2.21	-	-	-
Brick wall	3.00	-0.36	0.12	0.12

(a)

Material	Re{ε_r}	Im{ε_r}	tan(δ)	σ (S/m)
Glass	6.06	-1.07	0.18	0.35
Chipwood	2.88	-0.62	0.22	0.20
Plasterboard	2.02	-	-	-
Brick wall	3.58	-0.33	0.09	0.11

(b)

According to the measurement procedure, first the frequency response for the free-space situation is obtained and then the obstacle is placed perpendicularly between both antennas and the measurement repeated [8]. When measuring the free-space reference, the traveling electromagnetic wave covers the distance between both antennas, but when measuring the obstacle, the free-space distance is not the same, because the obstacle occupies part of the space. As the thickness of the obstacle is small compared to the total free-space distance, this hardly affects the fit of the model to amplitude measurements. However, as it is comparable to the wavelength, it has to be taken into account for phase calculations. When amplitude and phase transmissivity measurements are used, the model needs to be corrected, and the transmission coefficient with normal incidence should be written as in

$$T = \frac{(1-\Gamma^2)e^{-j\cdot k_s\cdot d_s}e^{-\alpha\cdot d_s}e^{j\cdot k\cdot d_s}}{(1-\Gamma^2 e^{-j\cdot 2\cdot k_s\cdot d_s}e^{-2\cdot\alpha\cdot d_s}e^{j\cdot 2\cdot k\cdot d_s})} \tag{2}$$

where k is the propagation constant across the free-space and the other parameters are the same as for (1). The model, including this correction, gives better agreement with the measured complex data.

IV. RESULTS

A Newton–Raphson algorithm was used to find the electromagnetic parameters that yield the best fit of measured data to the transmission coefficient model [9]. The complex permittivity of the materials were calculated as a function of frequency, for horizontal and vertical polarization. The real (solid line) and imaginary (dash-dotted line) components for the brick wall and the chipwood slab are plotted in Fig. 2. As can be seen these parameters exhibit some frequency dependence.

The mean values of the relative dielectric constant (ε_r), losses tangent $(\tan\delta)$ and conductivity (σ) for all the materials are summarized in Table I. Based on the calibration accuracy, the error for the dielectric constant is below 0.5% and, for the loss tangent below, $\pm 10^{-4}$. For the brick wall, which has an oriented internal structure, a polarization dependence in the dielectric constant can be observed.

V. CONCLUSION

An improvement on the commonly used internal multireflection model for transmission coefficients has been proposed and is used. The modification includes the effect of the slab thickness on the phase delay of the traveling wave. Using the proposed formulation, it is possible to reach a complete electromagnetic characterization from the amplitude and phase of the transmission coefficients. The computed relative dielectric constants depend on frequency and on the material. In the case of anisotropic materials, the dielectric constant also depends on the polarization.

REFERENCES

[1] R. O. Lamaire, A. Krishna, and P. Bhagwat, "Wireless LAN's and mobile networking: Standards and future directions," *IEEE Commun. Mag.*, pp. 86–94, August 1996.
[2] W. D. Burnside and K. W. Burgener, "High frequency scattering by a thin lossless dielectric slab," *IEEE Trans. Antennas Propagat.*, vol. AP-31, pp. 104–110, Jan. 1983.
[3] V. V. Varadan, R. D. Hollinger, D. K. Ghodgaonkar, and V. K. Varadan, "Free-space, broadband measurements of high-temperature, complex dielectric properties at microwave frequencies," *IEEE Trans. Instrum. Meas.*, vol. 40, pp. 842–846, Oct. 1991.
[4] D. K. Ghodgaonkar, V. V. Varadan, and V. K. Varadan, "Free-space measurement of complex permittivity and complex permeability of magnetic materials at microwave frequencies," *IEEE Trans. Instrum. Meas.*, vol. 39, pp. 387–394, Apr. 1990.
[5] ——, "A free- space method for measurement of dielectric constants and loss tangents at microwave frequencies," *IEEE Trans. Instrume. Meas.*, vol. 37, pp. 789–793, June 1989.
[6] P. A. Bello, "Characterization of randomly time-variant linear channels," *IEEE Trans. Commun. Syst.*, vol. CS-11, pp. 360–393, Dec. 1963.
[7] J. Lätheenmäki and T. Karttaavi, "Measurements of dielectric parameters of wall materials at 60 GHz Band," *Electron. Lett.*, vol. 32, no. 16, pp. 1442–1444, Aug. 1996.
[8] I. Cuiñas and M. G. Sánchez, "Measurement of transmission coefficients of radiowaves through building materials in the 5.8 GHz frequency band," in *Proc. 1999 IEEE AP-S Int. Symp.*, Orlando, FL, July 1999, pp. 1474–1477.
[9] I. Cuiñas, M. García Sánchez, and F. García Rodríguez, "Normal-incidence transmission of radiowaves through building materials in the 5.8 GHz frequency band," *Microwave Opt. Technol. Lett.*, pp. 7–12, Oct. 5, 1999.

Impedance and Polarization Characteristics of H and IHI Slot Antennas

Bradley G. Porter and Steven S. Gearhart

***Abstract*—Slot antennas can be end loaded to tune input impedance for use with active devices and to decrease overall slot length at a given resonant frequency. Cross polarization and impedance of end-loaded slots in an H configuration are analyzed in this letter. For an H antenna of approximately equal height and width, D-plane cross polarization was found to be −20 dB, and the resonant frequency decreased by 34% over a slot with a length equal to the width of the H. The cross polarization can be reduced with our new IHI configuration, which is introduced in this letter. Impedance at the second resonance can be tuned over a range of 26–82 Ω.**

***Index Terms*—Impedance matching, loaded antennas, polarization, slot antennas, spectral domain analysis.**

I. Introduction

End-loaded slot antennas can be used to reduce the length of a slot antenna without changing its resonant frequency [1]. Loading sections can be used to impedance tune slot antennas to the match the feedline or to match an active semiconductor device placed at the feed [2]. For slot-coupled patch applications, end-loaded slots result in less back radiation [3]. End-loaded slots are also suitable for large scanning angle phased arrays in which interelement spacing must be smaller than is permissible with conventional slot antennas [4].

If the end loading is symmetric, there is no cross polarization in the E-plane or H-plane. Hence, they have been considered for dual-polarized operation [3]. However, it is important to recognize that there will be some cross polarization in the D-plane ($\phi = 45^\circ$) of end-loaded slot antennas due to the perpendicular loading sections. In applications where high-polarization isolation is required (>20 dB) cross polarization due to the end-loaded sections cannot be ignored. This letter analyzes the cross polarization and impedance of the so-called H antenna for various end-load slot lengths (H heights) and introduces the new IHI antenna which reduces the cross polarization and allows further impedance tuning. Theoretical and experimental data are shown.

II. Theory

Adding conducting plates to the ends of a wire dipole antenna *capacitively* loads the dipole and alters its resonant frequency and resonant resistance [5]. Similarly, perpendicular slots connected to each end of a slot dipole antenna, *inductively* load it, and lower its resonant frequency and change its resistance. In this letter, the case of inductive loading of slot antennas in a ground plane with free-space on both sides of the ground plane is considered.

We use Galerkin's method in the spectral domain with electric field basis functions in the slot region, which are piecewise sinusoidal in one dimension and square in the other in a manner similar to [6]. A free-space Green's function is employed. Both x and y electric fields are considered for each slot region of the H and IHI slots. An x-directed electric field basis function is sinusoidal in the y-direction and a y-directed electric field basis function is sinusoidal in the x-direction.

Manuscript received May 14, 1998; revised May 3, 1999.

The authors were with the Microwave and Millimeter Wave Communications Laboratory, Department of Electrical and Computer Engineering, University of Wisconsin, Madison, WI 53706 USA. They are now with the Radar Design and Electronics Laboratory, Antenna and Microwave Department, Raytheon Company, Sudbury, MA 01776 USA (e-mail: bporter@ieee.org).

Publisher Item Identifier S 0018-926X(00)07702-4.

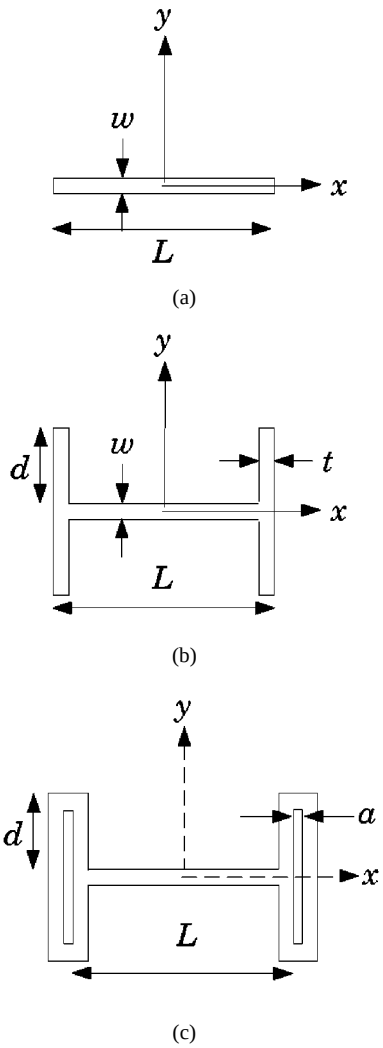

Fig. 1. Slot antenna geometries cut in a ground plane. (a) Slot. (b) H. (c) IHI.

III. Results

In this section, we will compare calculated input impedance and cross-polarization levels of a regular slot antenna, an H slot antenna, and the new IHI slot antenna. In addition, theoretical and measured resonant frequencies and resonant impedance are compared for all geometries considered.

A 48-mm-long 4-mm-wide magnetic dipole slot antenna [Fig. 1(a)] was constructed on a 0.25-mm woven glass substrate. End-loading slots were cut, as shown in Fig. 1(b). The woven glass dielectric was removed from the slot region to reduce dielectric loading for better agreement with the calculations which assume free space. The effect of the thin dielectric was small anyway since its thickness was less than 0.4% of a free-space wavelength. Coaxial cable delivered power to the center of the slot for impedance measurements, which were taken with an HP 8722C Network Analyzer. Figs. 2 and 3 show excellent agreement between the network analyzer impedance measurements and the moment method calculations. It is not surprising that the measured impedances have lower peaks since there are losses in the conducting ground plane that are not accounted for in the theory. Also, the network analyzer calibration did not take into account the losses of the 13-cm-long feed coax. Similar losses accounted for lower measured peaks in the recent literature [7]

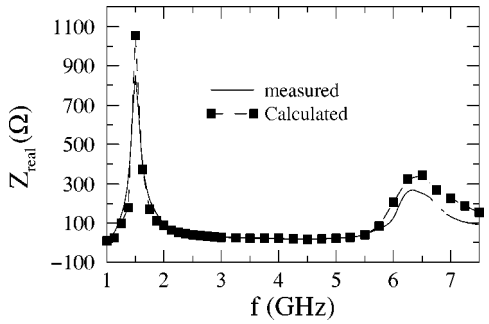

Fig. 2. Real (Z_{11}), H antenna, ($L = 48$ mm, $d = 18$ mm, $w = t = 4$ mm).

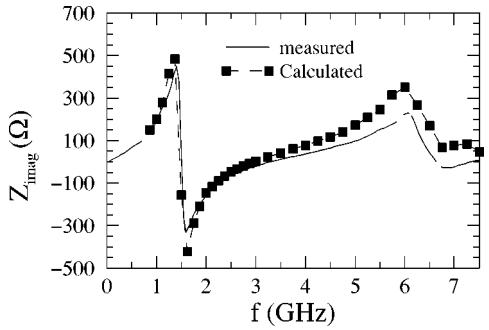

Fig. 3. Imag(Z_{11}). H antenna, ($L = 48$ mm, $d = 18$ mm, $w = t = 4$ mm).

Table I summarizes calculated and measured resonant frequencies and impedances along with calculated D-plane cross-polarization levels for various end-loading lengths. As shown in Table I, the inductive loading decreases both the resonant frequency and the resonant impedance. In each case, the width of the loading arms was equal to the width of the slot ($t = w = 4$ mm). There are a number of probable reasons for the slight discrepencies between impedance calculations and measurements. First, conductor losses are not accounted for in the theory; second, while a coaxial feed is a good approximation for the delta function feed in the theory, it is not exact; and third, insufficient computer resources to use enough basis functions to more accurately model the currents (basis functions in the main slot were 4 mm square; basis functions in the arms were no smaller than 1×1.33 mm).

Far-field radiation patterns are obtained from the Fourier transform of the electric field in the slot [8]. For the copolarized and cross-polarized field references, we use a slightly modified Ludwig's definition 2 [9]. We use an x-directed magnetic dipole as the reference field for copolar calculations and an x-directed electric dipole for cross-polar calculations when the source is in the x-directed slot.

There is no cross polarization in the E and H-planes because the currents in the parasitics are equal in opposite directions and the parasitic elements are placed symmetrically about the x and y axes, therefore, field contributions from them cancel in symmetry planes (E and H-planes). Fig. 4 shows that the D-plane cross-polarization level is not very high (-37 dB) for $d = 6$ mm; however, it increases to as much as -20 dB when $d = 18$ mm.

Polarimetric applications that require no less than -20 dB isolation between the two polarizations are limited to $d = 18$ for the H antenna. In any case, the antenna is now almost as wide as it is long and making the arms longer is not of any advantage when closely spaced printed circuits are required. However, we can simultaneously achieve more tuning and decrease the D-plane cross-polarization level by folding the the ends of the H back around to its center as shown in Fig. 1(c), which we denote as the IHI antenna. When this is done the resonant resistance, resonant frequency, and the cross-polarization decrease. For

TABLE I
CALCULATED AND MEASURED RESONANT RESISTANCE AND SECOND RESONANCE. CALCULATED PEAK D-PLANE CROSS-POLARIZATION LEVEL ($L = 48$ mm, $w = t = 4$ mm, $a = 1$ mm)

arm length (mm)	Resonant Resistance (calc/meas) (Ω)	Second Resonance (calc/meas) (GHz)	Peak D-plane x-pol (dB)	L+2d/λ_o (calc/meas)
d=0 (-)	82 / 63	4.44 / 4.71	<-100	0.71/0.75
d=6 (H)	52 / 47	3.63 / 3.95	-37	0.73/0.79
d=10 (H)	42 / 33	3.33 / 3.44	-29	0.76/0.78
d=18 (H)	28 / 25	2.95 / 3.27	-20	0.83/0.92
d=6 (IHI)	56 / 43	3.22 / 3.27	-39	0.64/0.65
d=10 (IHI)	39 / 34	2.96 / 3.24	-32	0.67/0.73
d=18 (IHI)	26 / 23	2.70 / 2.92	-24	0.76/0.82

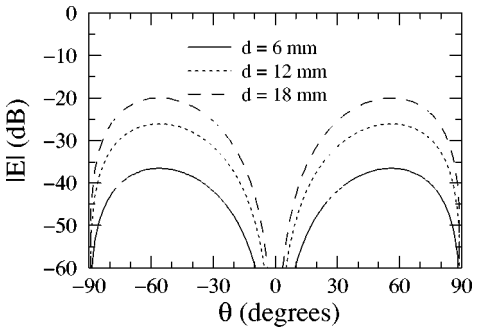

Fig. 4. Calculated H antenna D-plane cross-polarization patterns at second resonance for $L = 48$ mm, $w = t = 4$ mm.

$d = 18$ mm and $a = 1$ mm, the cross-polarization is reduced by 4 dB. Results for the IHI antenna are summarized in Table I along with those of the H antenna and the simple slot. For the IHI measurements, a thin dielectric strip supported the strip conductor in the end-loaded slots.

Table I shows that the resonant resistance decreases as the loading length d increases. It also shows that the H antenna with $d = 18$ mm and the IHI antenna with $d = 10$ mm have the same resonant frequency, but that the IHI has a resonant resistance closer to 50 Ω and has lower cross-polarization than the $d = 18$ mm H antenna.

IV. CONCLUSION

We have demonstrated a reduction in resonant resistance of slot antennas by the addition of perpendicular end-loading sections in an H configuration, and we have demonstrated that the length of the loading sections can be adjusted to tune the resonant resistance. In the case of the H antenna, polarization cannot be neglected when cross-polarization levels of less than -20 dB are desired and that cross polarization in the D-plane increases as the length of the tuning arms increase. More tuning can be achieved without increasing the D-plane cross-polarization level by folding the ends of the H into the IHI configuration, which is introduced in this letter.

REFERENCES

[1] V. Rathi, G. Kumar, and K. P. Ray, "Improved coupling for aperture coupled microstrip antennas," *IEEE Trans. Antennas Propagat.*, vol. 44, p. 1196, Aug. 1996.

[2] S. S. Gearhart and G. M. Rebeiz, "A monolithic 250 ghz Schottky-diode receiver," *IEEE Trans. Microwave Theory Tech.*, vol. 42, pp. 2504–2511, Dec. 1994.

[3] D. M. Pozar and S. D. Targonski, "Improved coupling for aperture coupled microstrip antennas," *Electron. Lett.*, vol. 27, no. 13, p. 1129, June 1991.

[4] F. Manshadi, "Small crossed-slot radiating elements for phased array applications," in *Proc. IEEE Antennas Propagat. Symp. Dig.*, London, ON, Canada, June 1991, p. 1828.
[5] R. E. Collin, *Antennas and Radiowave Propagation*. New York: McGraw-Hill, 1985.
[6] H.-C. Liu, T.-S. Horng, and N. G. Alexopoulos, "Radiation of printed antennas with a coplanar waveguide feed," *IEEE Trans. Antennas Propagat.*, vol. 43, p. 1143, Oct. 1995.
[7] T. M. Weller and L. P. Katehi, "Single and double folded-slot antennas on semi-infinte substrates," *IEEE Trans. Antennas Propagat.*, vol. 43, pp. 1423–1428, Dec. 1995.
[8] M. Kominami, D. Pozar, and D. Schaubert, "Dipole and slot elements and arrays on semi-infinite substrates," *IEEE Trans. Antennas Propagat.*, vol. AP-33, p. 600, June 1985.
[9] A. C. Ludwig, "The definition of cross polarization," *IEEE Trans. Antennas Propagat.*, vol. AP-21, pp. 116–119, Jan. 1973.

PO Near-Field Expression of a Penetrable Planar Structure in Terms of a Line Integral

Giuseppe Pelosi, Giovanni Toso, and Enrica Martini

***Abstract*—An exact line-integral representation of the physical optics (PO) field scattered in near zone by a penetrable planar structure illuminated by a plane wave is discussed.**

***Index Terms*—Dielectric bodies, electromagnetic diffraction, physical optics, planar objects.**

I. Introduction

The physical optics (PO) technique has been widely used for antennas and scattering problems involving structures, which are large in terms of a wavelength. The applications of the PO have been devoted essentially to perfectly conducting structures, but this technique is also applied for penetrable structures [1], [2]. The main drawback in the application of PO is the evaluation of a surface integral; the time required for this numerical integration is proportional to the surface of the structure under examination. Hence, for its implementation, converting surface integration into a line integration extended over the rim of the illuminated region is a really attractive solution.

The problem of reduction of a surface radiation integral to a line integral has been tackled by several authors. Different formulations have been proposed essentially depending on the scalar or vectorial nature of the involved fields; the light source (plane wave, dipole, etc.); the position of the observation point with respect to the illuminating source, the structure, and the geometrical optics (GO) shadow boundaries. So far, all the contributions (see, for instance, [3] and [4]) have been devoted to perfectly conducting structures. In this letter, we present an extension of the formulation proposed in [4] to the case of a penetrable planar structure illuminated by a plane wave.

II. Derivation of the Field-Integral Representation

The PO field scattered by a dielectric plate of arbitrary shape and negligible thickness in terms of wavelengths, illuminated by a plane wave, is given by the superimposition of the fields due to the free-space radiation of the PO equivalent currents distributed on the two faces. Despite the hypothesis of negligible thickness, made only to neglect the contributions due to the lateral surfaces, the procedure is not based on any sheet condition.

The contribution to the scattered field of each face can be expressed in the near zone using Kottler's representation [5], which involves surface integrals extended over the surface of the face and line integrals on its boundary C. Referring to Fig. 1, where a Cartesian system of coordinates with the origin located in the observation point $\boldsymbol{O}$ has been introduced, the PO field due to each face takes the following form [the time factor $\exp(j\omega t)$ is suppressed]:

$$\begin{aligned}\boldsymbol{E}^{\mathrm{PO}}(\boldsymbol{O}) = &-\iint_A \left[G(\boldsymbol{r})\hat{\boldsymbol{n}}\cdot\nabla\boldsymbol{F}_E(\boldsymbol{r}) - \hat{\boldsymbol{n}}\cdot\nabla G(\boldsymbol{r})\boldsymbol{F}_E(\boldsymbol{r})\right] dA \\ &+ \int_C G(\boldsymbol{r})\hat{\boldsymbol{t}}\times\boldsymbol{F}_E(\boldsymbol{r})\, dC \\ &+ \frac{j\zeta}{k}\int_C \hat{\boldsymbol{t}}\boldsymbol{F}_H(\boldsymbol{r})\nabla G(\boldsymbol{r})\, dC \end{aligned} \tag{1}$$

where ζ and k are the free-space intrinsic impedance and wave number, respectively, $\hat{\boldsymbol{t}}$ represents the unit tangent vector on C, positively oriented with respect to the unit normal $\hat{\boldsymbol{n}}$ on A ($\hat{\boldsymbol{n}} = \hat{z}$ on the upper face, $\hat{\boldsymbol{n}} = -\hat{z}$ on the lower face). Operator ∇ works on the coordinates of the observation point, $\boldsymbol{r}$ represents the vector from the observation point O to the integration point, $G(\boldsymbol{r})$ is the free-space scalar Green's function evaluated at $\boldsymbol{r}$. Vector operators $\boldsymbol{F}_E$ and $\boldsymbol{F}_H$ are defined in such a way that when we evaluate the contribution due to the upper face $\boldsymbol{F}_E(\boldsymbol{r}) = \boldsymbol{E}^i(\boldsymbol{r}) + \boldsymbol{E}^r(\boldsymbol{r})$, $\boldsymbol{F}_H(\boldsymbol{r}) = \boldsymbol{H}^i(\boldsymbol{r}) + \boldsymbol{H}^r(\boldsymbol{r})$; when, instead, we evaluate the contribution due to the lower face $\boldsymbol{F}_E(\boldsymbol{r}) = \boldsymbol{E}^t(\boldsymbol{r})$, $\boldsymbol{F}_H(\boldsymbol{r}) = \boldsymbol{H}^t(\boldsymbol{r})$, with $\boldsymbol{E}^i$, $\boldsymbol{E}^r$, $\boldsymbol{E}^t$ ($\boldsymbol{H}^i$, $\boldsymbol{H}^r$, $\boldsymbol{H}^t$) representing, respectively, the incident, the reflected and the transmitted electric (magnetic) field through the infinite dielectric slab with the same thickness and electromagnetic properties as those of the analyzed plate.

By applying the mathematical procedure illustrated in the Appendix based on the application of the dyadic divergence theorem to the volume V defined in Fig. 1, after tedious but straightforward calculations, one can demonstrate that (1) is exactly equivalent to the following expression:

$$\begin{aligned}\boldsymbol{E}^{\mathrm{PO}}(\boldsymbol{O}) = &\frac{\boldsymbol{F}_E(O)}{4\pi}\int_C \frac{\hat{\boldsymbol{t}}(\hat{\boldsymbol{q}}\times\hat{\boldsymbol{r}})}{r(1-\hat{\boldsymbol{q}}\cdot\hat{\boldsymbol{r}})}\, dC \\ &+ \frac{1}{4\pi}\int_C \hat{\boldsymbol{t}}\hat{\boldsymbol{r}}\times\int_0^1 \nabla\boldsymbol{F}_E(\alpha\boldsymbol{r})e^{-jk\alpha r}\, d\alpha\, dC \\ &+ \int_C G(\boldsymbol{r})\hat{\boldsymbol{t}}\times\boldsymbol{F}_E(\boldsymbol{r})\, dC \\ &+ \frac{j\zeta}{k}\int_C \hat{\boldsymbol{t}}\boldsymbol{F}_H(\boldsymbol{r})\nabla G(\boldsymbol{r})\, dC \end{aligned} \tag{2}$$

where $\hat{\boldsymbol{q}}$, as in [3], is any fixed unit vector with the property that $\hat{\boldsymbol{q}}\cdot\hat{\boldsymbol{n}} \leq \boldsymbol{0}$ and $\hat{\boldsymbol{q}}\cdot\hat{\boldsymbol{r}} \neq \boldsymbol{1}$ for each $\boldsymbol{r} \in \overline{A}$ ($\overline{A} = A \cup C$ is the closure of A). Due to the fact that the inner integral inside the double integral comparing in (2) reduces to a closed form, (2) involves only line integrals. Equation (2) represents the extension of [4, eq. (24)] to the case of penetrable plates illuminated by a plane wave.

III. Numerical Results

In order to illustrate the accuracy of the proposed formulation, the numerical results obtained by applying line integration have been compared with those obtained from the traditional surface integration. In

Manuscript received June 29, 1998; revised April 4, 2000.

The authors are with the Department of Electronics and Telecommunications, University of Florence, I50134 Florence, Italy (e-mail: pelosi@ingfi9.det.unifi.it).

Publisher Item Identifier S 0018-926X(00)07703-6.

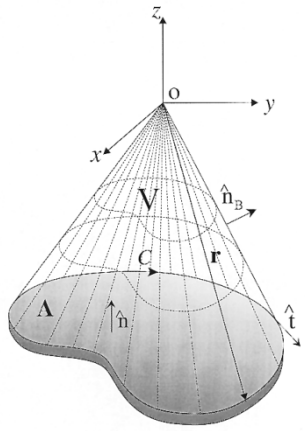

Fig. 1. Geometry for the problem.

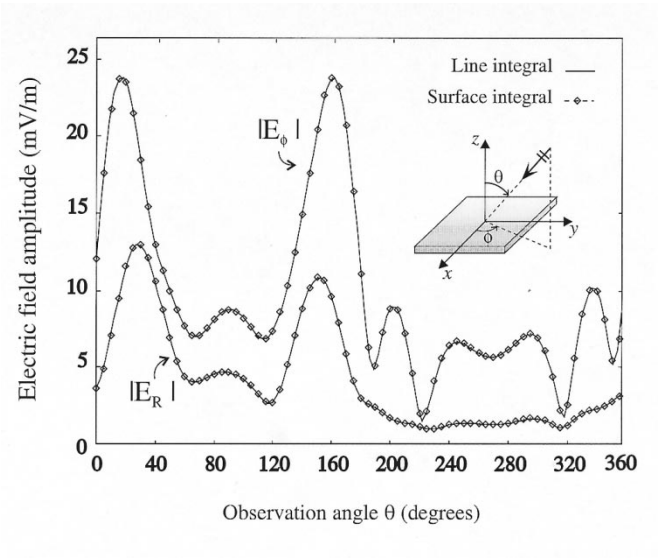

Fig. 2. Amplitudes of the ϕ- and R-components of the electric PO field scattered by a square dielectric plate (side $l = 2\lambda$, dielectric constant $\varepsilon_r = 3$, thickness $d = 0.05\lambda$). Continuous line: line integral technique; line with markers: surface integral technique.

particular, the amplitudes of the ϕ- and R-components of the PO electric field scattered by a square dielectric plate (side $l = 2\lambda$, dielectric constant $\varepsilon_r = 3$, thickness $d = 0.05\lambda$) are shown in Fig. 2. The incident plane wave is θ-polarized (with a unit amplitude electric field) and impinges on $\theta' = 45°$, $\phi' = 60°$. The observation point is located in the $\phi = 190°$ plane at a distance $R = 4\lambda$ from the center of the plate. As expected, a perfect agreement is observed between the continuous line (line integral) and the line with markers (surface integral). A similar agreement is found for the magnitude of the θ-component of the scattered electric field as well as for the phases.

To estimate the decrease in computation time with respect to surface integration, central processing unit (CPU) times required on a medium-power workstation to evaluate the PO scattered fields with the line and the surface integration were measured. These are reported in Fig. 3 as a function of the dimensions of the dielectric plate. The configuration under consideration is the same as that depicted in Fig. 2 and the observation distance with respect to the center of the plate is two times its side. It is important to note that the CPU times compared are relative to solutions with the same precision (a reference "exact" PO solution is obtained by using 40 sampling points per wavelength). The

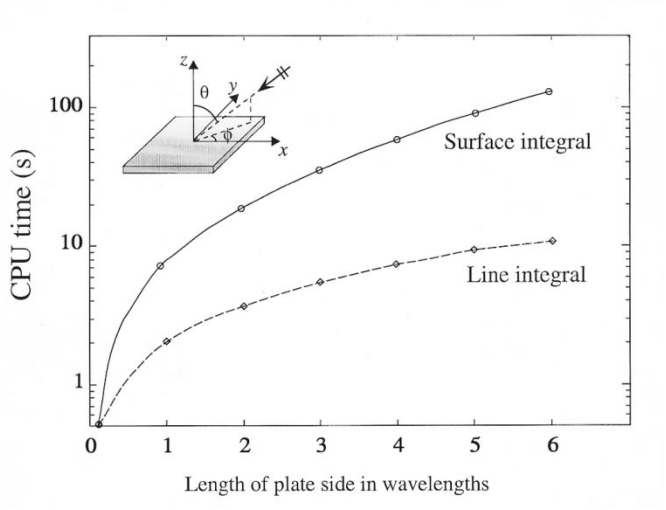

Fig. 3. CPU time required to evaluate the PO fields scattered by a square dielectric plate (dielectric constant $\varepsilon_r = 3$, thickness $d = 0.05\lambda$).

approach with line integration yields a significant decrease in computation time and time saving grows rapidly with the plate side.

APPENDIX

The surface integral in (1) can be considered as the flux through the surface A of the matrix function

$$\overline{\overline{\boldsymbol{V}}}(\boldsymbol{r}) = G(\boldsymbol{r})\nabla \boldsymbol{F}_E(\boldsymbol{r}) - \nabla G(\boldsymbol{r})\boldsymbol{F}_E(\boldsymbol{r}). \tag{A.1}$$

Consequently, it can be elaborated by using the dyadic theorem of divergence. We introduce a cone V with vertex at the observation point, basis A, and lateral surface B with outer normal $\hat{\boldsymbol{n}}_{\boldsymbol{B}}$ (see Fig. 1). By applying the divergence theorem to V we obtain

$$\iint_B \hat{\boldsymbol{n}}_{\boldsymbol{B}} \cdot \overline{\overline{\boldsymbol{V}}}(\boldsymbol{r})\, dB - \iint_A \hat{\boldsymbol{n}} \cdot \overline{\overline{\boldsymbol{V}}}(\boldsymbol{r})\, dA = \iiint_V \nabla \cdot \overline{\overline{\boldsymbol{V}}}(\boldsymbol{r})\, dV \tag{A.2}$$

where the negative sign before the second integral is due to the fact that $\hat{\boldsymbol{n}}$ is the inner normal. Consequently, we can replace the surface integral in (1) with the summation of a volume integral and a surface integral, extended to the lateral surface B of the cone. For what concerns the volume integral, by using the properties of the Green function and the fact that the GO field satisfies the Helmholtz equation in V, we can easily verify, with a procedure similar to that adopted in [4], that

$$\iiint_V \nabla \cdot \overline{\overline{\boldsymbol{V}}}(\boldsymbol{r})\, dV = \iiint_V \delta(r)\boldsymbol{F}_E(\boldsymbol{r})\, dV. \tag{A.3}$$

Due to the presence of the Dirac function, we have to consider only the value of $\boldsymbol{F}_E(\boldsymbol{r})$ at the observation point, so that the phase term disappears

$$\iiint_V \delta(r)\boldsymbol{F}_E(\boldsymbol{r})\, dV = \iiint_V \boldsymbol{F}_E(\boldsymbol{O})\delta(r)\, dV. \tag{A.4}$$

The integral of the Dirac function is then evaluated starting from the results published in [3] and [4] and we have

$$\iiint_V \nabla \cdot \overline{\overline{\boldsymbol{V}}}(\boldsymbol{r})\, dV = \frac{\boldsymbol{F}_E(\boldsymbol{O})}{4\pi} \int_C \frac{\hat{\boldsymbol{t}}(\hat{\boldsymbol{q}} \times \hat{\boldsymbol{r}})}{r(1 - \hat{\boldsymbol{q}} \cdot \hat{\boldsymbol{r}})}\, dC. \tag{A.5}$$

In order to reduce also the other surface integral of (A.2), i.e., the flux $\boldsymbol{I}_B$ of $\overline{\overline{\boldsymbol{V}}}(\boldsymbol{r})$ through the lateral surface B, to a line integral, it is suffi-

cient to consider that this flux can be written as a double integral, with the inner integral evaluated along the cone directrices, and the outer integral along the boundary of the plate. In particular, if $\boldsymbol{r}$ is the vector joining the observation point with a generic point of the boundary C, $\alpha\boldsymbol{r}$ describes a generatrix for $\alpha \in [0, 1]$ so that

$$\boldsymbol{I}_B = -\frac{1}{4\pi} \int_C \hat{\boldsymbol{t}} \cdot \hat{\boldsymbol{r}} \times \int_0^1 \nabla \boldsymbol{F}_E(\alpha \boldsymbol{r}) e^{-jk\alpha r}\, d\alpha\, dC. \tag{A.6}$$

In our case (plane wave excitation), the inner integral involves only exponential functions and can be easily evaluated in a closed form. In fact, for the incident, reflected and transmitted field we have to evaluate integrals of this kind

$$\boldsymbol{I} = \int_0^1 e^{-j\boldsymbol{k}\cdot\boldsymbol{r}\alpha} e^{-jk\alpha r}\, d\alpha = \frac{1 - e^{-j(\boldsymbol{k}\cdot\boldsymbol{r}+kr)}}{j\boldsymbol{k}\cdot\boldsymbol{r} + kr} \tag{A.7}$$

where $\boldsymbol{k}$ is the corresponding propagation vector.

The last consideration is true for all kinds of dielectric or magnetic slabs. In fact, the material characteristics affect only the reflection and transmission coefficients, which are constant with respect to the integration variables, so that the integrals can be evaluated in closed form without any restriction.

REFERENCES

[1] M. V. Vesnik and P. Ya. Ufimtsev, "An asymptotic feature of corner waves scattered by polygonal plates," *Electromagn.*, vol. 12, pp. 265–272, 1992.

[2] P. Corona, G. Manara, G. Pelosi, and G. Toso, "PO analysis of the scattering from polygonal flat-plate structures with dielectric inclusions," *J. Electromagn. Waves Applicat. (JEWA)*, vol. 14, pp. 693–711, 2000.

[3] J. S. Asvestas, "The physical optics field of an aperture on a perfectly conducting screen in terms of line integrals," *IEEE Trans. Antennas Propagat.*, vol. AP-34, pp. 1155–1159, Sept. 1986.

[4] P. M. Johansen and O. Breinbjerg, "An exact line integral representation of the physical optics scattered field: The case of a perfectly conducting polyhedral structure illuminated by electric Hertzian dipoles," *IEEE Trans. Antennas Propagat.*, vol. 43, pp. 689–696, July 1995.

[5] F. Kottler, "Diffraction at a black screen—Part II: Electromagnetic theory," *Progress Opt.*, vol. 6, pp. 331–377, 1967.